

Quantum evolution kernel : Machine learning on graphs with programmable arrays of qubits

Louis-Paul Henry,^{1,*} Slimane Thabet,^{1,*} Constantin Dalyac,^{1,2} and Loïc Henriët^{1,†}

¹*Pasqal, 2 avenue Augustin Fresnel, 91120 Palaiseau*

²*LIP6, CNRS, Sorbonne Université, 4 Place Jussieu, 75005 Paris, France*

(Dated: January 13, 2022)

The rapid development of reliable Quantum Processing Units (QPU) opens up novel computational opportunities for machine learning. Here, we introduce a procedure for measuring the similarity between graph-structured data, based on the time-evolution of a quantum system. By encoding the topology of the input graph in the Hamiltonian of the system, the evolution produces measurement samples that retain key features of the data. We study analytically the procedure and illustrate its versatility in providing links to standard classical approaches. We then show numerically that this scheme performs well compared to standard graph kernels on typical benchmark datasets. Finally, we study the possibility of a concrete implementation on a realistic neutral-atom quantum processor.

INTRODUCTION

Machine learning has now become part of the arsenal of almost all scientific fields. It has been successfully used in a wide range of applications, in particular whenever data can be represented as vectors (of potentially very high dimension). This is especially relevant in the analysis of image data and natural language processing.

In many fields such as chemistry [1, 2], bioinformatics [3, 4], social network analysis[5], computer vision[6], or natural language processing [7, 8], some observations have an inherent graph structure, requiring the development of specific algorithms to exploit the information contained in their structures. A large body of work exists in the classical machine learning literature, trying to study graphs through the use of *graph kernels* that are measures of similarity between graphs[9–12]. The richness of graphs’ structure gives them their versatility but poses a challenge in how one ought to proceed in order to extract the information they contain. The idea behind the graph kernel approach is very generic, and consists first in finding a way to associate any graph with a *feature vector* encapsulating its relevant characteristics (the *feature map*) and then to compute the similarity between those vectors, in the form of a scalar product in the feature space. The design of a kernel always comes down to a trade-off between capturing enough characteristics of the graph structure and not being too specific (so that graphs with similar properties yield similar results) while still being algorithmically efficient.

A lot of kernels have been introduced, each particularly fit to the study of particular types of problems or graph structures. The algorithmic complexity of most of these kernels makes them difficult to apply to the study of large graphs. For example, the *graphlets* subsampling and the random walk kernels that we will be using later scale

respectively as N^k and N^3 with the graph size N , and k the graphlet size (see B).

Previous work on quantum graph kernels has been done[13–15], both as generic algorithms introducing novel approaches inspired by quantum mechanics (Quantum graph neural networks[16], Quantum-walk kernels[17, 18]), as well as with a more specific computing platform in mind (e.g. using photonic devices[19]).

Here we propose a more versatile and easily scalable graph kernel based on similar ideas. The core principle is to encode the information about a graph in the parameters of a tunable Hamiltonian acting on an array of qubits and to measure a carefully chosen observable after an alternating sequence of *free* evolution (i.e. with this Hamiltonian) and/or parametrized pulses, similarly to what is done in the Quantum Approximate Optimization Algorithm (QAOA)[20], or after a continuously parametrization of the Hamiltonian, similarly to what can be done in optimal control[21]. This kernel can be realized with state-of-the-art QPUs, in particular with Rydberg atom processors [22–24], in which highly tunable Hamiltonians can be realized to encode a wide range of graph topologies with up to hundreds of qubits.

The paper is structured as follows. We first briefly introduce the reader to graph kernels in I. We then present the generic ideas of our quantum kernel in section II. An example of this kernel is detailed in III illustrating how it probes the underlying graph structure, and its versatility is illustrated in IV where it is related to other existing graph kernels. The performances of this kernel on real datasets are compared to other existing kernels in V and its implementation on neutral-atom processors is discussed and characterized in VI.

I. GRAPH KERNELS

One approach allowing to apply the tools of machine learning to data in the form of graphs is to find a way to represent each graph in an *embedding* vector space, and

* These authors contributed equally to this work

† loïc@pasqal.io

then measure the similarity between two graphs as the inner product between their representative vectors.

A graph kernel K constitutes such an inner product and therefore allows to perform machine learning tasks on graphs. More specifically, a graph kernel is a symmetric, positive semidefinite function defined on the space of graphs \mathbb{G} . Given a kernel K , there exists a map $\phi : \mathbb{G} \rightarrow \mathcal{H}$ into a Hilbert space \mathcal{H} such that $K(\mathcal{G}_1, \mathcal{G}_2) = \langle \phi(\mathcal{G}_1) | \phi(\mathcal{G}_2) \rangle$ for all $\mathcal{G}_1, \mathcal{G}_2 \in \mathbb{G}$ [25].

For completeness, we detail here two algorithms in which graph kernels can be used: Support Vector Machine (SVM) for classification (*i.e.* sorting data in categories) and Kernel Ridge Regression (KRR) for regression (*i.e.* the prediction of continuous values)[12, 26]. These methods have been successfully applied to data sets of graphs of up to a few dozen nodes [27].

A. Support Vector Machine

The SVM algorithm aims at splitting a dataset in two classes by finding the best hyperplane that separates the data points in the feature space, in which the coordinates of each data point (here each graph) is determined according to the kernel K .

For a training graph dataset $\{\mathcal{G}_i\}_{i=1\dots M}$, and a set of labels $\mathbf{y} = \{y_i\}_{i=1\dots M}$ (where $y_i = \pm 1$ depending on which class the graph \mathcal{G}_i belongs to), the dual formulation of the SVM problem consists in finding $\alpha_0 \in \mathcal{A}_C(\mathbf{y}) = \{\alpha \in [0, C]^M \mid \alpha^T \mathbf{y} = 0\}$ such that

$$\frac{1}{2} \alpha_0^T Q \alpha_0 - \mathbf{e}^T \alpha_0 = \min_{\alpha \in \mathcal{A}_C(\mathbf{y})} \left\{ \frac{1}{2} \alpha^T Q \alpha - \mathbf{e}^T \alpha \right\} \quad (1)$$

where \mathbf{e} is the vector of all ones, Q is a $M \times M$ matrix such that $Q_{ij} = y_i y_j K(\mathcal{G}_i, \mathcal{G}_j)$, and C is the penalty hyperparameter, to be adjusted. Setting C to a large value increases the range of possible values of α and therefore the flexibility of the model. But it also increases the training time and the risk of overfitting.

The data points for which $\alpha_i > 0$ are called support vectors (SV). Once the α_i are trained, the class of a new graph \mathcal{G} is predicted by the decision function, given by:

$$y(\mathcal{G}) = \text{sgn} \{ \langle \phi(\mathcal{G}) | \phi_0 \rangle \} \quad (2)$$

$$= \text{sgn} \left\{ \sum_{i \in SV} y_i \alpha_i K(\mathcal{G}, \mathcal{G}_i) \right\}, \quad (3)$$

with

$$\phi_0 = \sum_{i \in SV} y_i \alpha_i \phi(\mathcal{G}_i) \quad (4)$$

In this case, the training of the kernel amounts to finding the optimal feature vector ϕ_0 . It is worth noting that in many cases, equation (3) is evaluated directly, without explicitly computing ϕ_0 .

If the dataset is to be split into more than two classes, a popular approach is to combine several binary classification in a one-vs-one scheme[28]. This means that a classifier is constructed for each pair of classes in the dataset. Namely, for a dataset with n_c classes, $n_c(n_c - 1)/2$ classifiers will be constructed and trained (one for each pair of classes). This is the strategy that will be used here, whenever necessary.

B. Kernel Ridge Regression

The regression is similar to the classification task, but here the aim is to attribute a *continuous* value to each graph. Given a training graph dataset $\{\mathcal{G}_i\}_{i=1\dots M}$, and a set of labels $\mathbf{y} = \{y_i\}$ (that we assumed here to be in \mathbb{R}), the problem of linear regression consists in finding weights $\alpha = \{\alpha_i\}_{i=1\dots d}$ (where d is the dimension of the embedding space \mathcal{H}), such that for any new input graph \mathcal{G} , $y_\alpha(\mathcal{G}) = \alpha^T \phi(\mathcal{G})$. The solution α is found by minimizing

$$J(\alpha) = \frac{1}{2} \sum_{i=1}^M [y_\alpha(\mathcal{G}_i) - y_i]^2 + \frac{\lambda}{2} \alpha^T \alpha, \quad (5)$$

where λ is the regularization hyperparameter. This problem has a dual formulation by setting $\mathbf{a} = \Phi^T \alpha$ where Φ is the matrix whose rows are the embedded vectors $\phi(\mathcal{G}_i)$. By injecting the value of $\mathbf{a} = \{a_i\}_{i=1\dots M}$ in (5) the solution to the problem is given by

$$\mathbf{a} = (\mathbf{K} + \lambda I)^{-1} \mathbf{y} \quad (6)$$

where $\mathbf{K} = \{K(\mathcal{G}_i, \mathcal{G}_j)\}_{i,j} = \{ \langle \phi(\mathcal{G}_i) | \phi(\mathcal{G}_j) \rangle \}_{i,j}$ is the kernel matrix and \mathbf{y} is the vector of targets.

The prediction for a new input \mathcal{G} is then given by:

$$y(\mathcal{G}) = \sum_{i=1}^M a_i K(\mathcal{G}, \mathcal{G}_i) \quad (7)$$

The kernel presented here can be used for both classification and regression tasks, but only the former will be developed here.

II. QUANTUM EVOLUTION KERNEL

We now present a new Quantum Evolution (QE) Kernel, using the dynamics of an interacting quantum system as a tool to characterize graphs. The approach we propose consists in associating each graph \mathcal{G} with a probability distribution $\mathcal{P}_\mathcal{G}$, obtained by the measurement of an observable on a quantum system whose dynamics is driven by the topology of \mathcal{G} . The QE kernel between two graphs \mathcal{G} and \mathcal{G}' is then given as a distance between their respective probability distributions $\mathcal{P}_\mathcal{G}$ and $\mathcal{P}_{\mathcal{G}'}$.

A. Time-evolution

The time-evolution of a quantum state on a graph is a rich source of features for machine learning tasks such as the aforementioned classification and regression. Let us first detail the construction of the time-evolution.

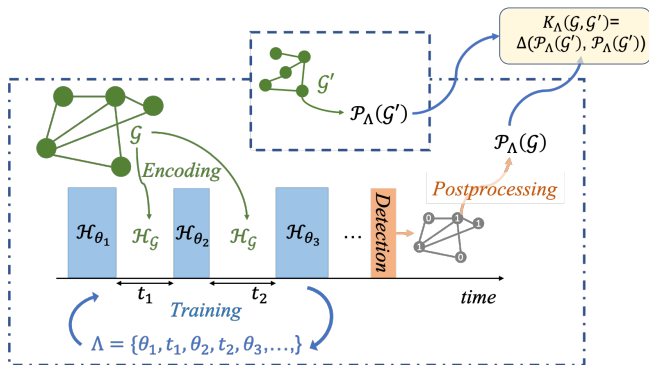


FIG. 1. Schematics of the feature map at the heart of the QE kernel. One first encodes an input graph \mathcal{G} into a Hamiltonian $\hat{\mathcal{H}}_{\mathcal{G}}$, which is used in a parametrized sequence, alternating evolution with $\hat{\mathcal{H}}_{\mathcal{G}}$ and pulses with Hamiltonian $\hat{\mathcal{H}}_{\theta_i}$. An observable is measured at the end of the pulse, yielding a bitstring. From this bitstring (or a list of bitstrings resulting from repeated iterations of this pulse), a probability distribution $\mathcal{P}_{\Lambda}(\mathcal{G})$ is extracted, out of which the graph kernel is computed, as a distance Δ on probability distributions. The precise form of the pulse sequence is determined through training on a graph data set.

We consider a system whose time-evolution is governed by the Hamiltonian $\hat{\mathcal{H}}_{\mathcal{G}}$, that can be any parametrized Hamiltonian whose topology of interactions is that of the graph under study. Given a graph $\mathcal{G} = (\mathcal{V}, \mathcal{E})$, one can take for example an Ising Hamiltonian of the form $\hat{\mathcal{H}}_{\mathcal{G}} = \hat{\mathcal{H}}_I = \sum_{(i,j) \in \mathcal{E}} \hat{\sigma}_i^z \hat{\sigma}_j^z$, or the XY Hamiltonian $\hat{\mathcal{H}}_{\mathcal{G}} = \hat{\mathcal{H}}_{XY} = \sum_{(i,j) \in \mathcal{E}} (\hat{\sigma}_i^+ \hat{\sigma}_j^- + h.c.)$. Those two Hamiltonians are analyzed here because they are ubiquitous spin models, that can be rather easily implemented on currently existing platforms (particularly in the case of neutral-atom processors, as described in VI). Depending on the problem at hand and the features of the graph one is trying to take into account, different Hamiltonians could be used¹.

We introduce then another Hamiltonian $\hat{\mathcal{H}}_{\theta}$, parametrized by a set of parameters θ , independent of \mathcal{G} and such that $[\hat{\mathcal{H}}_{\theta}, \hat{\mathcal{H}}_{\mathcal{G}}] \neq 0$, and use it to apply *pulses* to the system (i.e. letting it evolve with a coherent single-qubit driving $\hat{\mathcal{H}}_{\theta}$ ² for a duration τ ³).

The system starts in a predefined state $|\psi_0\rangle$. After an initial pulse with $\hat{\mathcal{H}}_{\theta_0}$, we alternatively let the system evolve with $\hat{\mathcal{H}}_{\mathcal{G}}$ (for a duration τ_i) and $\hat{\mathcal{H}}_{\theta_i}$ (as illustrated on Fig. 1). This time evolution can be summed up in the set of parameters

$$\Lambda = \{\theta_0, t_1, \theta_1, \dots, t_p, \theta_p\}. \quad (8)$$

In the remainder of the text, p will be referred to as the the depth (or the number of layers) of the procedure. After the time-evolution the system ends up in the state⁴

$$|\psi_f\rangle = \prod_{i=1}^p \left(e^{-i\hat{\mathcal{H}}_{\theta_i}} e^{-i\hat{\mathcal{H}}_{\mathcal{G}}t_i} \right) e^{-i\hat{\mathcal{H}}_{\theta_0}} |\psi_0\rangle \quad (9)$$

Remark: We present here a *layered* time-evolution scheme, but the idea can be easily extended to any kind of parametrized time-evolution $\hat{\mathcal{H}}(t)$ such that the final state is

$$|\psi_f\rangle = \exp \left[-i \int_0^{t_f} dt \hat{\mathcal{H}}(t) \right] |\psi_0\rangle \quad (10)$$

This can be thought of as taking the limit of an infinite number of layers. Analog quantum processing platforms are particularly well suited to the evaluation of this kind of quantities. Indeed in those systems, some of the parameters of the Hamiltonian can be continuously tuned (and it is often difficult to generate strictly piece-wise constant Hamiltonians).

B. Probability distribution

Once the system has been prepared in the final state $|\psi_f\rangle$, an observable $\hat{\mathcal{O}}$ is measured, to be used in the construction of the feature vector. We construct here two types of probability distributions that can be easily derived from quantum states, inspired by two standard types of measurements (power spectrum of an operator and histogram of measurements), but other ones could be considered as well.

1. Varying pulse sequence

The approach we consider consists in varying Λ , measuring $\hat{\mathcal{O}}$ several times for each Λ , so as to get $\bar{o}(\Lambda) = \langle \psi_f(\Lambda) | \hat{\mathcal{O}} | \psi_f(\Lambda) \rangle$, and then construct a probability distribution out of it.

¹ Synthetic Hamiltonians that can't be realized on quantum hardware could even be used in quantum-inspired classical algorithms implementing the QE kernel.

² In practice, $\hat{\mathcal{H}}_{\mathcal{G}}$ is not completely turned off during the pulses on

real hardware implementations, but can be neglected compared to $\hat{\mathcal{H}}_{\theta}$.

³ We can consider that $\tau = 1$ and include it in the definition of θ .

⁴ Throughout the paper, we set $\hbar = 1$

For example, if all the θ_i are kept fixed, and Λ varies in the duration $t = \sum_i t_i$, one could define $\mathcal{P}_{\mathcal{G}}^{\hat{\mathcal{O}}}$ as the (normalized) Fourier transform of $\bar{o}(t)$:

$$\mathcal{P}_{\mathcal{G}}^{\hat{\mathcal{O}}}(\Lambda) = (p_1, \dots, p_K)$$

$$p_k = \frac{1}{T} \left| \int_0^T dt e^{-2i\pi kt/T} \bar{o}(t) \right|. \quad (11)$$

As will be illustrated later, the Fourier components of $\bar{o}(t)$ (i.e. its power spectrum) can then be used as a fingerprint of \mathcal{G} .

2. Fixed pulse sequence

Another possible probability distribution is obtained from the tomography of the final state $|\psi_f\rangle$. It can be reconstructed from a series of measurements $\{m_1, \dots, m_M\}$ of the observable $\hat{\mathcal{O}}$ at the end of M repetitions of the exact same pulse sequence.

Let us note $\{\lambda_1, \dots, \lambda_K\}$, the eigenvalues of $\hat{\mathcal{O}}$ (i.e the possible outcomes of the measure), and $\{|o_1\rangle, \dots, |o_K\rangle\}$ the corresponding eigenstates. We can then associate to the graph a probability distribution

$$\mathcal{P}_{\mathcal{G}}^{\hat{\mathcal{O}}}(\Lambda) = (p_1, \dots, p_K), \text{ where } p_k = |\langle o_k | \psi_f \rangle|^2. \quad (12)$$

By constructing the histogram of the obtained values, one then effectively reconstructs the components of $|\psi_f\rangle$ in the eigenbasis of the operator.

Remark: Note that if some eigenvalues are degenerate, one would get instead $p_k = \sum_i \delta(\lambda_i - \lambda_k) |\langle o_i | \psi_f \rangle|^2$.

In practice, if K is large, one would resort to *binning* the values of λ_i , i.e. by defining a set of $K' < K$ intervals $\{I_k = [\tilde{\lambda}_k, \tilde{\lambda}_{k+1}]\}_{k=1, \dots, K'}$, with $\tilde{\lambda}_1 \leq \lambda_1$ and $\tilde{\lambda}_{K'+1} \geq \lambda_K$, such that $\mathcal{P}_{\mathcal{G}}^{\hat{\mathcal{O}}}(\Lambda) = (\tilde{p}_1, \dots, \tilde{p}_{K'})$, where

$$\tilde{p}_k = \frac{|\{m_i | m_i \in I_k\}|}{M} \stackrel{M \rightarrow \infty}{\equiv} \sum_{i | \lambda_i \in I_k} |\langle o_i | \psi_f \rangle|^2. \quad (13)$$

C. Graph kernel

We can now naturally define a graph kernel by computing the distances between the probability distributions. There are many choices of distances between probability distributions. We will here use the Jensen-Shannon divergence[29], which is commonly used in machine learning.

Given two probability distributions \mathcal{P} and \mathcal{P}' , the Jensen-Shannon divergence can be defined as

$$JS(\mathcal{P}, \mathcal{P}') = H\left(\frac{\mathcal{P} + \mathcal{P}'}{2}\right) - \frac{H(\mathcal{P}) + H(\mathcal{P}')}{2}, \quad (14)$$

where $H(\mathcal{P}) = -\sum_k p_k \log p_k$ is the Shannon entropy of \mathcal{P} . $JS(\mathcal{P}, \mathcal{P}')$ takes values in $[0, \log 2]$. In particular $JS(\mathcal{P}, \mathcal{P}) = 0$, and $JS(\mathcal{P}, \mathcal{P}') = \log 2$ is maximal if \mathcal{P} and \mathcal{P}' have disjoint supports.

For two graphs \mathcal{G} and \mathcal{G}' , and their respective probability distributions \mathcal{P} and \mathcal{P}' (computed as described above), we define the graph kernel as

$$\mathcal{K}_{\mu}(\mathcal{G}, \mathcal{G}') = \exp[-\mu JS(\mathcal{P}, \mathcal{P}')] \in [2^{-\mu}, 1]. \quad (15)$$

The kernel is then positive by construction. Throughout the paper, we will set $\mu = 1$, but it might be helpful to adjust this value to improve the results.

The parameter Λ is determined through training on a dataset containing graphs whose class is known.

In the case of SVM, the outcome of training consists in the optimal value of Λ as well as the corresponding support vector coefficients α_i defining the best hyperplane splitting the data set. The class of a new graph \mathcal{G} is then predicted by computing its probability distribution $\mathcal{P}_{\mathcal{G}}^{\hat{\mathcal{O}}}(\Lambda)$ and then computing its kernel values with respect to graphs in the training dataset, according to (3).

III. ISING QUANTUM EVOLUTION KERNEL AT DEPTH $p = 1$

As an illustration, we now derive an expression in a simple case, inspired by Ramsey interferometry, where the probability distribution is the Fourier transform of the total occupation of an Ising system, after a *Ramsey sequence*, comprising a free evolution of duration t between two conjugate global pulses $\hat{\mathcal{H}}_{\theta}$ and $\hat{\mathcal{H}}_{-\theta} = \hat{\mathcal{H}}_{\theta}^*$. This example will highlight how relevant characteristics of a graph can be captured, even in this very basic setting, by acting uniformly on all the qubits encoding it.

A. Description of the Kernel

Let us consider a graph $\mathcal{G} = (\mathcal{V}, \mathcal{E})$ and a set of $N = |\mathcal{V}|$ qubits interacting with the Ising Hamiltonian $\hat{\mathcal{H}}_{\mathcal{G}}$, and subject to the *mixing* Hamiltonian $\hat{\mathcal{H}}_{\theta}$, characterized by a single parameter $\theta = \{\vartheta\}$, defined as

$$\hat{\mathcal{H}}_{\mathcal{G}} = \sum_{(i,j) \in \mathcal{E}} \hat{\sigma}_i^z \hat{\sigma}_j^z \equiv \hat{\mathcal{H}}_I \text{ and } \hat{\mathcal{H}}_{\theta} = \vartheta \sum_{i \in \mathcal{V}} \hat{\sigma}_i^y \equiv \vartheta \hat{\mathcal{H}}_1, \quad (16)$$

where $\hat{\sigma}^y$ and $\hat{\sigma}^z$ are the Pauli spin operators. The qubit are initially in the *empty* product state

$$|\psi_0\rangle = \bigotimes_{i \in \mathcal{V}} |0\rangle \equiv |0 \dots 0\rangle, \quad (17)$$

and we consider the case of a single layer $p = 1$, with parameters $\Lambda = \{\theta, t, -\theta\}$, as defined in (9), so that the

final state of the system is

$$|\psi_\vartheta(t)\rangle \equiv |\psi_f(\Lambda)\rangle = e^{i\vartheta\hat{H}_1} e^{-it\hat{H}_G} e^{-i\vartheta\hat{H}_1} |\psi_0\rangle. \quad (18)$$

We choose here to measure the total occupation of the system $\hat{O} \equiv \hat{n} = \sum_{i \in \mathcal{V}} (1 + \sigma_i^z)/2$, so that

$$\bar{o}(t) \equiv n_\vartheta(t) = \langle \psi_\vartheta(t) | \hat{n} | \psi_\vartheta(t) \rangle \quad (19)$$

Finally, the probability distribution is computed according to (11)⁵. In practice, the Fourier transform of the output of the quantum device would be computed over a finite time-interval T . But we will consider here that it is large enough (as compared to the spectrum of the model), and focus on the $T \rightarrow \infty$ limit. In such a procedure, the first pulse brings each qubit in a coherent superposition of the two basis states. During the free evolution of this state, different components of the superposition acquire relative phases, which depend, for each qubit, on the number of neighbors of the corresponding node of the underlying graph \mathcal{G} . The final pulse maps coherences onto populations, and the analysis of the signal in Fourier space then enables to probe the connectivity structure of the graph, as we show below.

B. Analytical results

The diagonal nature of the Ising Hamiltonian in the computational basis makes it possible to reach closed formulas, and this should serve as a nice illustrative example. Details of the calculations can be found in A 1.

If a graph \mathcal{G} contains $m_{\mathcal{G}}(\kappa)$ vertices of degree κ , then $\bar{o}(t)$ reduces to⁶

$$n_\vartheta(t) = 2 \cos^2 \vartheta \sin^2 \vartheta \sum_{\kappa \geq 0} m_{\mathcal{G}}(\kappa) w_\kappa(t), \quad (20)$$

$$\text{with } w_\kappa(t) = \Re \left\{ 1 - (\cos^2 \vartheta + e^{it} \sin^2 \vartheta)^\kappa \right\}. \quad (21)$$

The probability distribution is then given by

$$p_0^{(\infty)} = 2 \cos^2 \vartheta \sin^2 \vartheta \sum_{\kappa \geq 0} m_{\mathcal{G}}(\kappa) (1 - \cos^{2\kappa} \vartheta), \quad (22)$$

$$p_{k>0}^{(\infty)} = (\sin \vartheta)^{2(1+k)} \sum_{\kappa \geq k} \binom{\kappa}{k} m_{\mathcal{G}}(\kappa) (\cos \vartheta)^{2(\kappa+1-k)}.$$

This can be very efficiently computed. Indeed, since $m_{\mathcal{G}}(\kappa) = 0$ for $\kappa > \kappa_{\max}$, where $\kappa_{\max} < N - 1$ is the maximum degree of the graph, one can introduce a set of N vectors $\{\mathbf{V}_k\}_{k=0, \dots, N-1}$, of dimension N , defined as

$$\begin{aligned} \mathbf{V}_0 &= 2 \cos^2 \vartheta \sin^2 \vartheta \left\{ 1 - \cos^{2\kappa} \vartheta \right\}_{\kappa \geq 0} \\ \mathbf{V}_{k>0} &= (\cos \vartheta)^{2(1-k)} (\sin \vartheta)^{2(1+k)} \left\{ \binom{\kappa}{k} (\cos \vartheta)^{2\kappa} \right\}_{\kappa \geq 0}. \end{aligned}$$

⁵ $\mathcal{P}_{\mathcal{G}}^{\hat{O}}(\Lambda) = \mathcal{P}_{\mathcal{G}}^{\hat{n}}(\theta)$ is defined up to a normalization constant.

⁶ This sum actually finite as $m_{\mathcal{G}}(\kappa) = 0$ for any $\kappa > \kappa_{\max}$.

For a given graph \mathcal{G} , one then just needs to compute the degree histogram vector

$$\mathbf{m}_{\mathcal{G}} = \{m_{\mathcal{G}}(\kappa)\}_{\kappa \geq 0}, \quad (23)$$

so that the components of the feature vector are obtain via a simple scalar product :

$$p_k^{(\infty)} = \mathbf{m}_{\mathcal{G}} \cdot \mathbf{V}_k. \quad (24)$$

The results are illustrated in Fig. 2, for two small sets of graphs generated with the Erdős–Rényi model[30], for different edge probability $\rho = 0.35$ and $\rho = 0.65$. The different classes of graphs are nicely captured in this simple case (as one would expect, since the Erdős–Rényi parameter p can be accurately evaluated from the degree histogram, when the graphs become large enough). Indeed, the distance obtained between graphs of the same category is 100 times smaller than between graphs of different classes.

This simple formula may seem to somehow defeat the purpose of a quantum graph kernel (as no speedup is to be gained from a quantum machine). But this is only a very simple example. In a more generic case — and in particular in the case described in V — the evolution would be more intricate and no simple analytic formula is expected to be computable.

IV. CONNECTION TO RANDOM-WALK KERNELS

Before we delve into the benchmarking of the QE kernel on a specific case in V, let us illustrate how it is very general, specifically how it can be connected to already existing kernels, with a proper choice of the Hamiltonian and/or observable.

A. Steady-state random walk kernel

Random-walk based kernels can be more efficiently computed than graphlet-based ones[31], and have therefore been extensively used in the literature. We show here how the QE kernel can be linked to these kernels.

We still work in the case of the Ising Hamiltonian, but we now measure separately the occupation of each site (i.e. $\hat{O} = \hat{n}_i$), and computes the probability distribution $\mathcal{P}_{\mathcal{G}}(\theta) = \{p_0^{(i)}\}_{i \in \mathcal{V}}$, with $p_0^{(i)} \equiv \overline{n_i(t)}$ the time-averaged occupation of site i . It can be expressed as

$$p_0^{(i)} = 2 \cos^2 \vartheta \sin^2 \vartheta (1 - \cos^{2\kappa_i} \vartheta) \underset{\vartheta \rightarrow 0}{\approx} 2\vartheta^4 \{\kappa_i\}, \quad (25)$$

where κ_i is the degree of vertex i .

This distribution is then equivalent to that of the classical steady-state random walk[32], in which the time spent on each vertex (or the probability of visiting it) is used as a component of the feature vector.

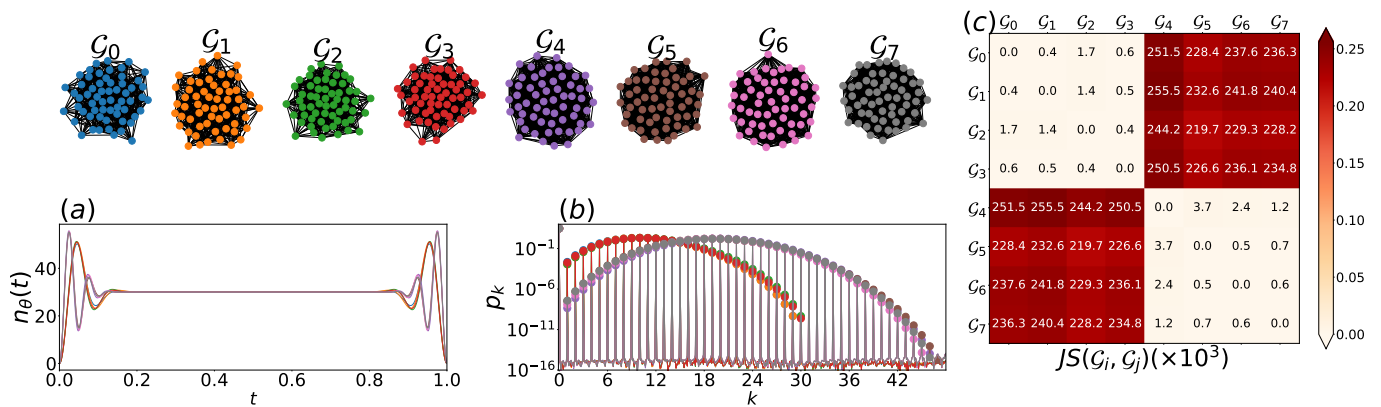


FIG. 2. (color online) Illustration of the Ising QE kernel at depth $p = 1$, for 8 random Erdős–Rényi graphs of $N = 60$ nodes, with edge probability respectively $\rho = .35$ ($\mathcal{G}_0, \dots, \mathcal{G}_3$) and $\rho = .65$ ($\mathcal{G}_4, \dots, \mathcal{G}_7$), and $\vartheta = \pi/4$. (a) One period of the time dependence of the density as expressed in (20), the color of each graph is the same as the corresponding plot. (b) Probability distribution extracted from this procedure. The lines are the Fourier Transform of $n_\theta(t)$ (with a finite value of the total time T), while the dots are given by (22). Two types of distributions are clearly emerging, corresponding to the two classes of graphs. (c) The Jensen-Shannon divergence computed from p_k . The color represents the value of the Jensen-Shannon divergence between the two corresponding graphs (it is 0 on the diagonal, by definition). Bright colors correspond to similar graphs, while darker (red) color correspond to larger values of the divergence (and therefore dissimilar graphs). This groups nicely the graphs of the same class.

B. Quantum walks

It has been shown that, for certain types of graphs, a classical random-walk fails to explore efficiently the system, while a quantum walk would be able to do it [33]. We now briefly examine the case where the graph Hamiltonian is chosen to be H_{XY} , and highlight its connection to random-walk kernels.

1. Quantum-walk kernel

The XY Hamiltonian $\hat{\mathcal{H}}_{XY}$ preserves the total occupation number. We introduce $H_n = \text{span} \{ |\sigma\rangle \mid \sum_{i \in \mathcal{V}} \sigma_i = n \}$ the subspace of states with occupation n . $\hat{\mathcal{H}}_{XY}$ is then block-diagonal, with each block acting on one of the H_n . We will note $\hat{\mathcal{H}}_n$ the restriction of $\hat{\mathcal{H}}_{XY}$ to this subspace.

In particular, the matrix representing $\hat{\mathcal{H}}_1$ is (isomorphic to) the adjacency matrix of \mathcal{G} . If one is able to prepare the system in an initial state $|\psi_0\rangle$ that only has components in H_1 , the evolution of the system with $\hat{\mathcal{H}}_{XY}$ then corresponds to a random walk of a single (potentially delocalized) particle on the graph. If one adds a longitudinal field term $\sum_i \kappa_i \hat{n}_i$ (with κ_i the degree of vertex i), the Hamiltonian becomes the Laplacian of the graph. From the dynamics of this system, one can then reconstruct the *quantum-walk kernel* [17, 18], from the histograms of the local density operators \hat{n}_i .

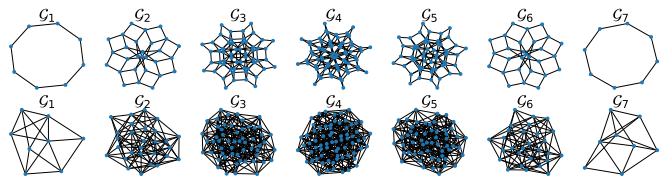


FIG. 3. The sequence of occupation graphs \mathcal{G}_n from a loop (*top row*) and random (*bottom row*) initial graph $\mathcal{G} \equiv \mathcal{G}_1$. As the occupation is increased, both the number of vertices and the number of edges grow exponentially. In the case of the periodic chain, the \mathcal{G}_n s retain the rotational/permutation symmetry of \mathcal{G} .

2. Generic occupation graphs

The XY Hamiltonian presents further applications. Let us consider again a graph $\mathcal{G} = (\mathcal{V}, \mathcal{E})$, containing $N = |\mathcal{V}|$ nodes and $M = |\mathcal{E}|$ edges. For any value of n , $\hat{\mathcal{H}}_n$ describes the random walk on \mathcal{G} of n particles with hardcore interactions. Let us define an effective graph \mathcal{G}_n , with $\binom{N}{n}$ vertices corresponding to the $\binom{N}{n}$ Ising configurations σ with n 1s, such that $(\sigma, \sigma') \in \mathcal{E}_n$ if $\langle \sigma | \hat{\mathcal{H}}_n | \sigma' \rangle = 1$. The matrix representing $\hat{\mathcal{H}}_n$ is then (isomorphic to) the adjacency matrix of \mathcal{G}_n .

We show the various \mathcal{G}_n for a periodic chain graph as well as for an arbitrary graph, both of size $N = 8$ (Fig. 3). The computation of the Quantum Evolution kernel is very difficult for a classical computer, as the size of

$\mathcal{G}_n = (\mathcal{V}_n, \mathcal{E}_n)$ grows quickly with $n \leq N/2^7$:

$$|\mathcal{V}_n| = \binom{N}{n} \text{ and } |\mathcal{E}_n| = M \binom{N-1}{n-1} = \frac{Mn}{N} |\mathcal{V}_n|. \quad (26)$$

On a quantum device, however, if one is able to prepare the system in a state with a defined occupation n , it is then straightforward to compute the QE kernel for one of the \mathcal{G}_n . One would just need to make sure to use a mixing Hamiltonian $\hat{\mathcal{H}}_\theta$ that also preserves the occupation number (e.g. by combining \mathcal{H}_{XY} with a longitudinal-field term).

It is worth noting that for a given graph \mathcal{G} , the density of \mathcal{G}_n — defined as $d_n = 2|\mathcal{E}_n|/|\mathcal{V}_n|(|\mathcal{V}_n| - 1)$ — decays rapidly as $n \rightarrow N/2$.

3. Full Hamiltonian dynamics

In the case where the initial state overlaps with several occupation number sectors, it is harder to get a proper description in terms of random walks, highlighting the difference between classical and quantum walks. However, a link to the random-walk properties of the different \mathcal{G}_n can still be made. We will illustrate this in a setting similar to that of III, with the depth set to $p = 1$, and the parameters $\Lambda = \{\theta, t, -\theta\}$, and the graph Hamiltonian $\hat{\mathcal{H}}_{\mathcal{G}} = \hat{\mathcal{H}}_{XY}$. The observable that is measured is again the total occupation $\hat{\mathcal{O}} = \sum_i \hat{n}_i$. After a sequence with a free evolution of duration t , the expected total occupation is given by

$$n(t) = 2N(\cos \vartheta)^2(\sin \vartheta)^2 - 2(\cos \vartheta)^{2N+2} \sum_{\sigma \in \{0,1\}^N} \varrho_{n_\sigma}(t), \quad (27)$$

with

$$\varrho_{n_\sigma}(t) = (\tan \vartheta)^{2n_\sigma} \sum_{\substack{p,q \geq 0 \\ \delta=0,1}} \left\{ (-1)^\delta (-t^2)^{p+q+\delta} \times \frac{l_{2p+\delta}(\sigma)}{(2p+\delta)!} \sum_{\tilde{\sigma} \in \mathcal{F}_\sigma^-} \frac{l_{2q+\delta}(\tilde{\sigma})}{(2q+\delta)!} \right\}, \quad (28)$$

where $l_p(\sigma)$ is the number of random walks of length p in \mathcal{G}_{n_σ} starting at σ , and $\mathcal{F}_\sigma^- = \{\tilde{\sigma} \in \mathcal{G}_{n_{\sigma-1}} | \langle \tilde{\sigma} | \hat{\sigma}_i^- | \sigma \rangle = 1\}$ is the set of configurations obtained by flipping one of the $\sigma_i = 1$ to 0. This expression combines properties of random-walks on different occupation graphs, illustrating how various occupation sectors are involved in QE kernels based on the XY Hamiltonian.

One may then expect the resulting classifier to capture intricate properties that a random-walk on a single sector or a classical walk would miss.

V. BENCHMARKING OF THE QUANTUM EVOLUTION KERNEL

The scheme presented in III requires the measurement of the time-dependence of the expectation value of an operator. In most existing quantum computing platform, this would require a prohibitive number of measurements, in order to have sufficient statistics on enough Fourier components. In order to circumvent this issue, we now turn to a more promising scheme, requiring fewer measurements. In this setting, one reconstructs the histogram of the observable in the final state, in a *fixed pulse sequence*, as briefly mentioned in II B 2.

We consider again a $\mathcal{G} = (\mathcal{V}, \mathcal{E})$ and a set of $N = |\mathcal{V}|$ qubits. The observable to be measured is the *Ising energy* associated with the graph :

$$\hat{\mathcal{O}} = \hat{\mathcal{H}}_I = \sum_{(i,j) \in \mathcal{E}} \hat{\sigma}_i^z \hat{\sigma}_j^z \quad (29)$$

The goal is to sample $\hat{\mathcal{O}}$ in the final state $|\psi_f\rangle$, obtained after p layers :

$$|\psi_f(\Lambda)\rangle = \prod_{i=1}^p \left(e^{-i\hat{\mathcal{H}}_{\theta_i}} e^{-i\hat{\mathcal{H}}_{\mathcal{G}t_i}} \right) e^{-i\hat{\mathcal{H}}_{\theta_0}} |\psi_0\rangle, \quad (30)$$

with $\Lambda = \{\theta_0 = \pi/4, t_1, \theta_1, \dots, t_p, \theta_p\}$ fixed for a given dataset, and determined by the training procedure.

By repeating the measurement $\langle \psi_f | \hat{\mathcal{O}} | \psi_f \rangle$ many times, one reconstructs the tomography of ψ_f in the eigenbasis $\{|o_i\rangle\}_i$ of $\hat{\mathcal{O}}$. Here, because of the choice of observable, this basis coincides with the computational basis $(\{|o_i\rangle\}_i = \{|\sigma_i\rangle | \sigma_i \in \{0,1\}^N\})$. Indeed, for

$$|\psi_f(\Lambda)\rangle = \sum_i \psi_f^{(i)} |o_i\rangle, \quad (31)$$

the result of the measurement of $\hat{\mathcal{O}}$ gives $E_\sigma = \sum_{(i,j) \in \mathcal{E}} \sigma_i \sigma_j$ with probability $p_i = |\psi_f^{(i)}|^2$. The probability distribution that this methods tries to reconstruct is closely related to $\mathcal{P}_{\mathcal{G}}(\Lambda) = \left\{ |\langle \psi_f(\Lambda) | \sigma_i \rangle|^2 \right\}_i$ ⁸. It would take an exponentially growing number of measurements to evaluate this exact distribution. However, as the results of this section and of VI will show, sufficient information can be obtained from the histogram of the measured values, when the size of the bins is small enough. For a given bin width $\delta\epsilon$, the resulting probability distribution from a series of M measurements $\{\tilde{o}_1, \dots, \tilde{o}_M\}$ is then

$$\begin{aligned} \{\mathcal{P}_{\mathcal{G}}^{(\delta\epsilon)}(\Lambda)\}_i &= \frac{1}{M} \sum_j \chi_i(\tilde{o}_j) \\ &\equiv \sum_j \chi_i(o_j) |\langle \psi_f(\Lambda) | \sigma_j \rangle|^2 \end{aligned} \quad (32)$$

⁷ Because of the particle-hole symmetry \mathcal{G}_n and \mathcal{G}_{N-n} are equivalent.

⁸ Note that this is only true if the eigenvalues of $\hat{\mathcal{O}}$ are non-degenerate.

where χ_i is the indicator function of the i -th bin of the histogram. We now proceed to characterize this kernel. To this end, we consider the graph Hamiltonian to be either the Ising Hamiltonian \mathcal{H}_I (diagonal in the computational basis), or the XY Hamiltonian $\hat{\mathcal{H}}_{XY}$ (non-diagonal in the computational basis). We follow a procedure similar to that described in [19] to benchmark the graph kernel.

We tested the protocol on a graph classification task on several datasets and we compare the results with other graph kernels. Each graph kernel is associated with a Support Vector Machine, and the score is the accuracy, namely the proportion of graph in the test set that are attributed the correct class. We perform a grid search on the hyperparameter C (defined in IA) in the range $[10^{-3}, 10^3]$ and we select the value with the best score. For each value of the parameters Λ , the obtained accuracy is averaged over 10 repetitions of the following cross-validation procedure: the dataset is first randomly split into 10 subsets of equal size. The kernel is then tested (*i.e.* its accuracy is measured) on each of these 10 subsets, after having been trained on the 9 other subsets. The accuracy resulting from this split is then the average accuracy over the 10 possible choices of test subset.

The datasets are taken from the repository of the Technical University of Dortmund [27]. Attributes and labels of nodes and edges are ignored. Because the simulation of large quantum systems is algorithmically costly, only graphs between 1 and 16 nodes are considered. In the case of the Fingerprint dataset, only the classes 0, 4 and 5 are considered, because each other class constitute at most $\sim 7\%$ of the dataset (to be compared to the $\sim 25\%$ of each of the classes 0, 4 and 5). Table I summarizes the characteristics of each dataset after preprocessing.

Dataset	samples	classes	samples per classes
IMDB-MULTI	1185	3	371, 403, 411
IMDB-BIN	499	2	239, 260
PTC_FM	234	2	135, 99
PROTEINS	307	2	82, 225
NCI1	361	2	282, 79
Fingerprint	1467	3	515, 455, 597

TABLE I. Characteristics of the datasets after preprocessing, keeping graphs containing less than 16 nodes, and classes with enough representatives.

The parameter Λ is trained by Bayesian Optimization. The function to optimize is the accuracy score averaged on all cross-validation splits, and a gaussian surrogate function is trained with a Matérn Kernel (see Appendix C for more details). At each step, the surrogate function is minimized by sampling 5000 points. The computation time depends on the dataset and the type of Hamiltonian used. The number of evaluations is then chosen so as to keep the total evaluation times of the order of a few hours across datasets.

We compared the QE kernels to the Graphlet Subsampling (GS) kernel[34, 35] and the Random Walk (RW)

kernel[36]. The procedure used to compute these kernels are described in B. In the GS kernel, we used 1000 samples and perform a grid search over the graphlet subsizes from 3–6. For the RW kernel, we performed a grid-search over the weight hyperparameter in $[0.001, 0.01]$. The values of the penalty hyperparameter C have been restricted to $[10^{-3}, 10^{-1}]$ to limit the computation time. The simulations of classical kernels have been done with the `grakel` library [37].

All the results are summarized in table II. For all datasets, at least one quantum kernel is better than the best classical kernel. The depth of the evolution plays an important role, since increasing the number of layers for the Ising evolution almost always leads to a better score. This confirms the fact that adding more layers allows for the capture of richer features. For IMDB-MULTI and Fingerprints, the 8-layer Ising scheme performances seem worse than those of the 4-layer Ising. It is an artifact due to the incomplete convergence of the optimization. Indeed, since those datasets are bigger, less evaluations of the function were allowed in our computational budget.

Our results show that a graph kernel based on the time-evolution of a quantum system can lead to an efficient classification of graphs. Since many different QE kernels can be built, one immediate avenue to improvement would be to try to build a better kernel by combining them. This is the idea behind multikernel learning[38]. The main appeal to this approach here is that it could efficiently combine quantum and classical computing, by determining classically the optimal combination among kernels that were trained on a QPU (see D for more details).

VI. IMPLEMENTATION ON NEUTRAL-ATOM PLATFORMS

Several platforms have been developed recently, aiming at simulating quantum spin models: ions [39], polaritons [40] and neutral atoms [41]. Those quantum processors (QPU) would be particularly well suited to an implementation of the Quantum Evolution kernel. We detail here the case of a programmable array of qubits made of neutral atoms.

A. Description of the platform

Arrays of individual neutral atoms trapped in optical tweezers [41–50] have emerged as a promising platform for quantum information processing. By promoting the atoms to so-called Rydberg states, they behave as huge electric dipoles and experience dipole-dipole interactions that map into spin Hamiltonians. The spins undergo various types of interactions depending on the Rydberg states involved in the process, leading to different Hamiltonians [41], as illustrated in Fig 4. The most common configuration is the Ising model, illustrated in 4(a) which

Dataset	Ising ₁ (150)	Ising ₄ (2000)	Ising ₈ (6000)	XY ₄ (2000)	GS	RW
IMDB-MULTI	46.8 ± 4.4	48.1 ± 4.4	47.7 ± 4.4	47.5 ± 4.5	40.9 ± 3.5	45.2 ± 3.4
IMDB-BIN	69.0 ± 6.1	71.6 ± 5.7	71.8 ± 5.4	70.6 ± 5.6	66.5 ± 5.9	67.8 ± 6.5
PTC_FM	62.5 ± 7.9	65.8 ± 7.9	66.0 ± 7.6	65.2 ± 8.2	61.5 ± 8.9	59.4 ± 7.8
PROTEINS	73.3 ± 1.2	74.5 ± 2.6	76.0 ± 5.3	74.8 ± 3.7	73.3 ± 1.2	73.3 ± 1.2
NCII	78.1 ± 0.8	78.6 ± 3.2	80.1 ± 3.5	78.8 ± 4.8	78.1 ± 0.8	78.1 ± 0.8
Fingerprint	58.6 ± 2.0	60.2 ± 3.2	60.1 ± 3.3	60.1 ± 3.3	57.9 ± 3.3	59.9 ± 2.2

TABLE II. Comparison of the accuracy of the graph kernel on various data sets. The average over all cross-validation splits and the standard deviation associated is displayed. These values were obtained measuring the Ising energy after p layers with an Ising graph Hamiltonian (Ising _{p}) or an XY Hamiltonian (XY _{p}). Next to each model is indicated a rough approximation of the number of evaluations. The quantum kernel in the Ising setting outperforms the other kernels considered. The resources needed to evaluate the score on bigger data sets (sl e.g. IMDB-MULTI and Fingerprint) allow for less evaluations. Models with more layers could be tested in the case of Ising, which is faster to simulate than XY.

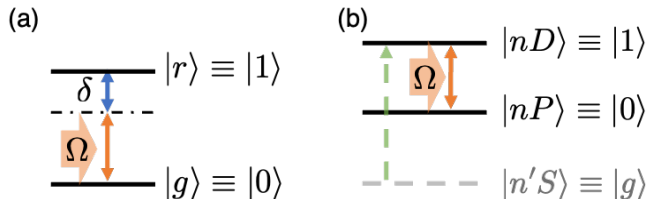


FIG. 4. Implementation of quantum spin models with neutral atoms. In the Ising case (a), the spin states $|0\rangle$ and $|1\rangle$ correspond to a ground state $|g\rangle$ and a rydberg state $|r\rangle$ of the atom. The amplitude Ω of the pumping laser determines the transverse-field term in the Ising model, and the detuning to resonance δ induces a longitudinal-field term. In the XY case (b), the spin states correspond to two dipolar rydberg state $|nP\rangle$ and $|nD\rangle$. The atoms are first brought from a ground state $|g\rangle$ to $|nD\rangle$. A microwave driving between $|nP\rangle$ and $|nD\rangle$ can additionally generate tunable σ^x and σ^z terms.

is obtained when the $|0\rangle$ state is one of the ground states $|g\rangle$ and the $|1\rangle$ state a Rydberg state $|r\rangle$ [23, 51–53]. In this case, a van der Waals interaction between atoms arises due to non-resonant dipolar interactions, and leads to an interaction term of the form $C_6/(r_{ij}^6)n_i n_j$, where $n_j = (1 + \sigma_j^z)/2$ represents the Rydberg state occupancy of the spin j . The coupling between two spins i and j depends on the inverse of the distance between them r_{ij} to the power of 6, and on a coefficient C_6 relative to the Rydberg state.

The XY Hamiltonian is another example of a spin model that one can realize on this platform. It naturally appears when the spin states $|0\rangle$ and $|1\rangle$ are two Rydberg states with a finite dipolar moment (such as e.g. $|nP\rangle$ and $|nD\rangle$ [54, 55], or $|nS\rangle$ and $|nP\rangle$ [56]). In that case, a resonant dipole-dipole interaction occurs, resulting in the creation of a term $2C_3/(r_{ij}^3)(\sigma_i^x \sigma_j^x + \sigma_i^y \sigma_j^y)$ between atoms. This term describes a coherent exchange of spin states, transforming the pair state $|01\rangle$ into $|10\rangle$. This interaction scales as the inverse of the distance r_{ij} to the power of 3 and depends on a coefficient C_3 relative to the Rydberg states.

A driving field can be used to implement the rotations. By tuning the amplitude, the phase and the frequency of the driving, one can engineer any *global* single-qubit

operation (or, in terms of spin models, any uniform magnetic field Ω so as to add a term $\sum_{i \in \mathcal{V}} \Omega \cdot (\hat{\sigma}_i^x, \hat{\sigma}_i^y, \hat{\sigma}_i^z)$ to the Hamiltonian).

As the interaction strength depends on the distance between atoms, only local graphs can be embedded in this platform. As such, only databases containing local graphs could be used. Note that an additional position-dependent detuning term could be used for graphs with labeled nodes.

B. Illustration on a simple dataset

As an example, we emulate the computation of the graph kernel described in V, and apply it to a simple dataset containing graphs that are small enough to be computationally tractable with classical computers, ahead of implementation on a real hardware.

These simulations are done using the *pulser* library [57]. In these, the characteristics of the laser acting on the atoms (amplitude and frequency) are set at each time, tuning the Hamiltonian seen by the atoms. The interaction Hamiltonian is determined by the spatial distribution of the atoms, that can be tuned to any arbitrary geometry (current hardware implementation is limited to 2D, but even 3D configurations could be assembled similarly).

1. Details of the implementation

We focus here on the dataset Fingerprint. We used for that purpose a subset (referred to as Fingerprint* in the remainder of the text) consisting of 200 graphs from this dataset, restricted to graphs up to 12 nodes. As before, only the categories 0, 4 and 5 were considered.

With the notation presented in II, the chosen graph and mixing Hamiltonians are

$$\hat{\mathcal{H}}_G = \sum_{i>j} J_{ij} \hat{\sigma}_i^z \hat{\sigma}_j^z \quad \hat{\mathcal{H}}_\theta = \tau \hat{\mathcal{H}}_G + \frac{\Omega_0 \tau}{2} \sum_{i \in \mathcal{V}} \hat{\sigma}_i^x, \quad (33)$$

where here the coupling $J_{ij} = C_6/R_{ij}^6$ coupling between atoms i and j decays with the distance R_{ij} between them.

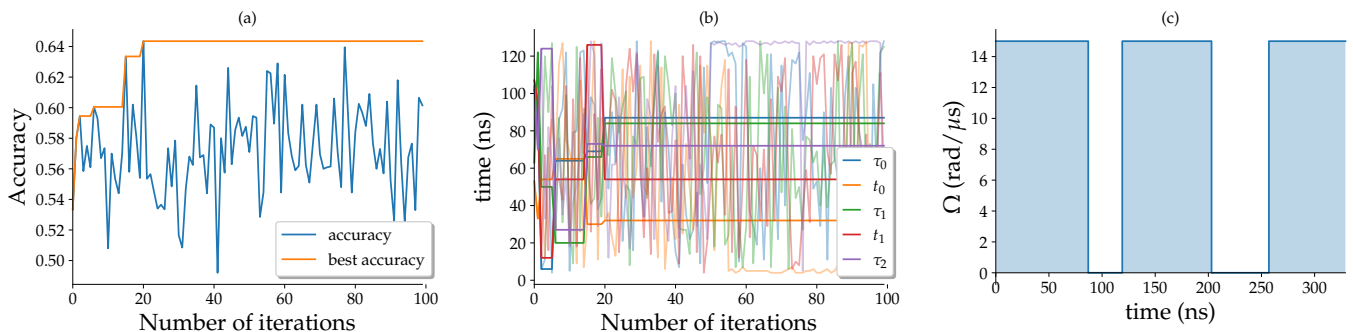


FIG. 5. (a) Accuracy of the quantum graph kernel, in the case of the Ising Graph Hamiltonian, with $p = 2$ layers, as a function of the number of bayesian optimization, with a false positive and false negative detection error of $\epsilon = 0.05$ and $\epsilon' = 0.05$ respectively. The blue curve is the accuracy obtained from the parameters set each iteration, while the orange curve represents the best accuracy obtained up to each iteration. After ~ 20 iterations, the accuracy of the kernel goes from $\sim .55$ to $\sim .64$, its maximal value reached in this case. Further iterations don't lead to any improvement. (b) The corresponding values of the parameters Λ of the pulse. Faint lines are the values at each iteration while the solid lines are the values reaching the best accuracy. The values keep fluctuating, suggesting that it may be possible to further train the kernel. (c) Optimal amplitude Ω of the pulse sequence obtained after training on Fingerprint*.

The dataset contains coordinates of the nodes such that the graphs are locals, we used them to position the atoms in the register. A rescaling is applied such that the minimum distance between the atoms is $5 \mu\text{m}$. The amplitude is kept constant and set to the highest value reachable by the QPU ($\Omega_0 = 15 \text{ rad}/\mu\text{s}$). The detuning is set here to $\delta = 0$, so that a mixing pulse is then characterized by a single parameter $\theta_i = \tau_i$. We chose an architecture of 2 layers of alternating Rabi pulses ($\Omega = \Omega_0$, $\delta = 0$) and free evolution, so that $\Lambda = \{\tau_0, t_0, \tau_1, t_1, \tau_2\}$. The values of the durations $\{\tau_0, t_0, \tau_1, t_1, \tau_2\}$ are the variables to be optimized. In order to get a realistic pulse for the existing hardware, with a finite response and coherence times, we impose that $\tau_0, t_0, \tau_1, t_1, \tau_2 > 4 \text{ ns}$ and $T = \tau_0 + t_0 + \tau_1 + t_1 + \tau_2 < 500 \text{ ns}$.

We consider first the case where the various sources of noise are ignored, and determine the optimal values for Λ . Using the same cross-validation scheme as in V, we determine the obtained accuracy of the kernel, and compare it to the GS and RW kernels on the same dataset, as summarized in table III. The standard deviation on the accuracy is estimated via cross-validation, similarly to what was done in V. As before, the quantum kernel reaches a higher accuracy than the reference kernels.

2. Sensitivity to noise

One of the key problematic of quantum computing is the robustness to noise. In order to quantify the effect of the noise, we set the false positive and false negative error rates to $\epsilon = 0.05$ and $\epsilon' = 0.05$ respectively (in accordance to conservative estimates for currently existing devices). This type of noise is independent of the duration of the evolution, and for short enough times (less than a few microseconds), it is expected to dominate over other sources of imperfection (decoherence in particular).

In a real implementation, the probability distribution would be reconstructed from a finite number of noisy measurements. In order to emulate this effect, we estimate the kernel 100 times on different sets of 10000 measurements. For each of these 100 estimations, the accuracy is again evaluated via the same 10-fold cross-validation procedure as before. The average accuracy is reported in III, alongside those of other kernels on the same dataset. With this kind of noise, the estimated accuracy is not significantly altered as compared to the noiseless case, and still outperforms the two comparison kernels.

Dataset	QE(0)	QE(0.05)	GS	RW
Fingerprint*	64.0 \pm 8.7	63.0	48.2 \pm 8.9	52.0 \pm 5.8

TABLE III. Accuracy reached on the reduced data set Fingerprint*, by the quantum evolution kernel in the case of a 2-layer scheme (as described in the text) without noise (QE(0)) and with detection error (QE(0.05)), as well as that of the Graphlet Subsampling (GS) and Random Walk (RW) kernels. The average of accuracy over the splits and the associated standard deviation are noted (see table II). For the noisy kernel, the value is the average over all 100 kernel estimates, and thus the standard deviation cannot be directly compared to that of other the kernels in the table.

Let us now briefly analyze the convergence of the optimization. As illustrated in figure 5 (a), most of the accuracy increase is obtained after only a few iterations of optimization (~ 20 in the example illustrated here). It might be possible to reach a higher value, but at the cost of much longer computations. This would go beyond the scope of such an illustrative study, and the value reached here already surpasses the GS and RW kernels. The corresponding parameters of Λ can be seen in figure 5(b) The resulting best pulse is shown in figure 5 (c), consisting of three mixing pulses of similar duration (87, 84 and 72 ns respectively, corresponding to pulses with $\vartheta \approx 0.4\pi$,

0.4π and $\pi/3$ in the non-interacting case described in V), alternating with shorter free evolutions (32 and 54 ns).

Let us now turn to the alteration of the kernel due to detection errors. For each pair of graphs \mathcal{G}_i and \mathcal{G}_j , the resulting value of the kernel $K_{\epsilon, \epsilon'}(\mathcal{G}, \mathcal{G}')$ averaged over several measurements is compared to what was obtained in the noiseless case. To this end, the relative difference between those values is introduced :

$$\delta K_{ij}(\epsilon, \epsilon') = \left| 1 - \frac{K_{\epsilon, \epsilon'}(\mathcal{G}, \mathcal{G}')}{K_{0,0}(\mathcal{G}_i, \mathcal{G}_j)} \right|. \quad (34)$$

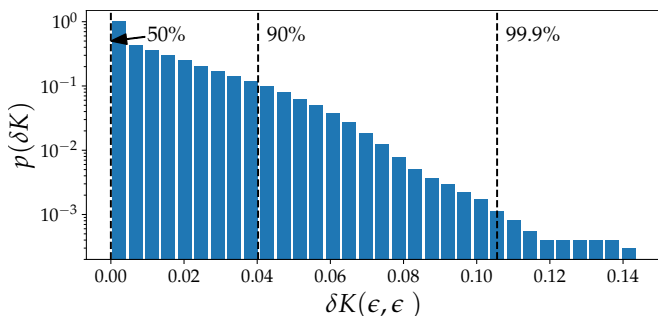


FIG. 6. Cumulative distribution of the relative change of the values of the kernel in the presence of detection error (set to $\epsilon = \epsilon' = .05$), as defined in (34) (note the logscale of the y-axis). The average is performed over 100 estimations of the set of feature vectors, each one estimated with 10,000 measurements. The dashed vertical lines represent the 0.5, .9 and .999 quantiles.

The histogram of the values of $\delta K_{ij}(\epsilon, \epsilon')$ obtained across 100 training sequences over the data set Fingerprint* are represented in figure 6. As indicated by the arrow, for roughly half of the pairs of graphs, the relative error is below machine precision, and the distribution decays rapidly when the discrepancy increases (the relative change due to noise is above 10% for only $\sim 0.13\%$ of them).

This is consistent with the estimated accuracy in the noisy case, that stays close to the one of the noiseless kernel, and that still surpasses that of GS and RW (as shown in III).

CONCLUSION

We proposed a new procedure for building graph kernels and analyze graph-structured data than can be implemented on quantum devices. This Quantum Evolution kernel is very flexible as it was illustrated on a few examples. We showed that QE is on par with state-of-the-art graph kernels in terms of accuracy. We were able to benchmark its expected performances on a neutral-atom quantum device, via simulation of the dynamics on small graphs, and show that the performances of the kernel are stable against detection error. Our proposal can be readily tested on state-of-the-art neutral atom platforms.

These platforms may be limited to smaller graphs (up to ~ 100 nodes), but quantum-inspired algorithms have been introduced for a wide range of problems[58, 59], and it has been suggested that a significant speed-up could be gained by implementing variations of near-term quantum computing algorithms running on GPUs.

In a short-term perspective, the most exciting follow up will be to implement a QE kernel on a real quantum machine.

In the meantime, a lot can still be done on the theory side. We focused on the layered time-evolution scheme, using Ising or XY Hamiltonians. But, as mentioned earlier in the text, there might be cases or platforms for which a continuous approach *à la* optimized control might yield interesting results. We also only discussed the case of an Ising or XY graph Hamiltonian, but here as well, a lot has yet to be done in order to understand which Hamiltonian to use. More synthetic/abstract choices (using more than two -body interactions for example) could widen the range of application of this approach. Similarly, designing the right observable to measure or the best probability distribution to construct from the dynamics of the system are also potential sources of improvement. This includes the use of multikernel learning, to combine different kernels built from the same sequence of measurements (and their associated bitstrings) on the final states. Finally, understanding the effect of the various sources of noise on the performances of the kernel will be essential, as some of them might even contain information on the underlying graph.

ACKNOWLEDGMENTS

We thank Lucas Leclerc, Antoine Browaeys, Thierry Lahaye, Romain Fouilland and Christophe Jurczak for useful discussions. It was granted access to the HPC resources of CINES under the allocation 2019-A0070911024 made by GENCI. It was also supported by region Ile de France through the Pack Quantique (PAQ).

Appendix A: Computation of the time-dependent expectation value of diagonal operators in the Ising case

We provide here more details about analytical results in a few tractable cases. First, in the simplest case where $p = 1$, with a uniform Ising model without linear term, then in the case of the most generic Ising model, and finally in the case where quadratic observables are measured.

1. Detailed computation in the case $p = 1$

We detail here the computations in the case of the Ising Hamiltonian with a depth of $p = 1$, leading to (20).

For a given $\sigma \in \{0,1\}^N$, we note $|\sigma\rangle = \bigotimes_i |\sigma_i\rangle$, and $n_i = \sum_{i \in \mathcal{V}} \sigma_i$, and we introduce the mixing operator

$$\begin{aligned} \hat{P}_\vartheta^\dagger &= \exp(-i\hat{\mathcal{H}}_\vartheta) \equiv \prod_i \hat{P}_{\vartheta,i}^\dagger \\ &= \prod_i [\cos \vartheta \mathbb{1} + \sin \vartheta (\hat{\sigma}_i^+ - \hat{\sigma}_i^-)], \end{aligned}$$

so that

$$\hat{P}_\vartheta^\dagger |\psi_0\rangle = \sum_{\sigma \in \{0,1\}^N} (\cos \vartheta)^{N-n_\sigma} (\sin \vartheta)^{n_\sigma} |\sigma\rangle.$$

The Ising Hamiltonian $\hat{\mathcal{H}}_I$ (16) is diagonal in the computational basis ($\hat{\mathcal{H}}_I |\sigma\rangle = E_\sigma |\sigma\rangle$), therefore

$$e^{-i\hat{\mathcal{H}}_I t} \hat{P}_\vartheta^\dagger |\psi_0\rangle = \sum_{\sigma \in \{0,1\}^N} (\cos \vartheta)^{N-n_\sigma} (\sin \vartheta)^{n_\sigma} e^{-iE_\sigma t} |\sigma\rangle.$$

Finally the state that is measured is

$$\begin{aligned} |\psi_\vartheta(t)\rangle &= e^{i\vartheta\hat{\mathcal{H}}_1} e^{-it\hat{\mathcal{H}}_G} e^{-i\vartheta\hat{\mathcal{H}}_1} |\psi_0\rangle \\ &= \sum_{\sigma \in \{0,1\}^N} (\cos \vartheta)^N (\tan \vartheta)^{n_\sigma} e^{-iE_\sigma t} \bigotimes_i \hat{P}_{\vartheta,i} |\sigma_i\rangle \end{aligned}$$

The final measurement can be written as

$$\begin{aligned} n(t) &= (\cos \vartheta)^{2N} \sum_{\sigma, \sigma' \in \{0,1\}^N} \left\{ e^{-i(E_\sigma - E_{\sigma'})t} (\tan \vartheta)^{n_\sigma + n_{\sigma'}} \right. \\ &\quad \left. \times \sum_{\mu \in \{0,1\}^N} n_\mu \prod_{i=1}^N \langle \sigma'_i | \hat{P}_{\vartheta,i}^\dagger | \mu_i \rangle \langle \mu_i | \hat{P}_{\vartheta,i} | \sigma_i \rangle \right\}. \end{aligned} \quad (\text{A1})$$

We note that

$$\langle \mu_i | \hat{P}_{\vartheta,i} | \sigma_i \rangle = \cos \vartheta \delta_{\mu_i, \sigma_i} + \sin \vartheta (\delta_{\mu_i, \sigma_i - 1} - \delta_{\mu_i, \sigma_i + 1}),$$

so that we get the following table

$(\mu_i, \sigma_i, \sigma'_i)$	$\langle \sigma'_i \hat{P}_{\vartheta,i}^\dagger \mu_i \rangle \langle \mu_i \hat{P}_{\vartheta,i} \sigma_i \rangle$
(0, 0, 0), (1, 1, 1)	$\cos^2 \vartheta$
(0, 1, 1), (1, 0, 0)	$\sin^2 \vartheta$
(0, 1, 0), (0, 0, 1)	$\cos \vartheta \sin \vartheta$
(1, 1, 0), (1, 0, 1)	$-\cos \vartheta \sin \vartheta$

(A2)

We can then write

$$\begin{aligned} \prod_{i=1}^N \langle \sigma'_i | \hat{P}_{\vartheta,i}^\dagger | \mu_i \rangle \langle \mu_i | \hat{P}_{\vartheta,i} | \sigma_i \rangle &= \\ (\cos \vartheta)^{2N} (\tan \vartheta)^{n_\neq + 2n_1} (\tan \vartheta)^{2(n_\mu^{(0)} - n_\mu^{(1)})} (-1)^{n_\mu^{(\neq)}}, \end{aligned}$$

where

$$\begin{aligned} n_1 &= \sum_{i \in \mathcal{V}} \sigma_i \sigma'_i \equiv |\{i \in \mathcal{V} | \sigma_i = \sigma'_i = 1\}| \\ n_0 &= \sum_{i \in \mathcal{V}} (1 - \sigma_i)(1 - \sigma'_i) \equiv |\{i \in \mathcal{V} | \sigma_i = \sigma'_i = 0\}| \\ n_\neq &= \sum_{i \in \mathcal{V}} [\sigma_i(1 - \sigma'_i) + \sigma'_i(1 - \sigma_i)] \equiv |\{i \in \mathcal{V} | \sigma_i \neq \sigma'_i\}| \\ n_\mu^{(1)} &= \sum_{i \in \mathcal{V}} \sigma_i \sigma'_i \mu_i \equiv |\{i \in \mathcal{V} | \sigma_i = \sigma'_i = 1 \neq \mu_i\}| \\ n_\mu^{(0)} &= \sum_{i \in \mathcal{V}} \sigma_i \sigma'_i \mu_i \equiv |\{i \in \mathcal{V} | \sigma_i = \sigma'_i = 0 \neq \mu_i\}| \\ n_\mu^{(\neq)} &= \sum_{i \in \mathcal{V}} [\sigma_i(1 - \sigma'_i) + \sigma'_i(1 - \sigma_i)] \mu_i \\ &\equiv |\{i \in \mathcal{V} | \sigma_i \neq \sigma'_i \wedge \mu_i = 1\}|. \end{aligned}$$

Therefore

$$\begin{aligned} \sum_{\mu \in \{0,1\}^N} n_\mu \langle \sigma'_i | \hat{P}_{\vartheta,i}^\dagger | \mu_i \rangle \langle \mu_i | \hat{P}_{\vartheta,i} | \sigma_i \rangle &= \\ \delta_{0, n_\neq} [n_0 (\sin \vartheta)^2 + n_1 (\cos \vartheta)^2] - \delta_{1, n_\neq} \cos \vartheta \sin \vartheta, \end{aligned}$$

and

$$\begin{aligned} n(t) &= 2N \sin^2 \vartheta \cos^2 \vartheta \\ &\quad - 2(\cos \vartheta)^{2N+2} \sum_{\sigma \in \{0,1\}^N} (\tan \vartheta)^{2n_\sigma} \sum_{i | \sigma_i = 1} \cos(\Delta_{\sigma,i} t), \end{aligned}$$

where $\Delta_{\sigma,i} = E_\sigma - E_{\sigma'(i)}$ where $\sigma'(i)$ is the configuration obtained from σ by flipping i . We can transform this sum, remarking that

$$\begin{aligned} \sum_{\sigma \in \{0,1\}^N} (\tan \vartheta)^{2n_\sigma} \sum_{i | \sigma_i = 1} \cos(\Delta_{\sigma,i} t) &= \\ \sum_{i \in \mathcal{V}} \sum_{n=0}^N (\tan \vartheta)^{2n} \sum_{\substack{\sigma | n_\sigma = n \\ \sigma_i = 1}} \cos(\Delta_{\sigma,i} t). \end{aligned}$$

We note κ_i the degree of node i . For two given integers $\omega \leq \kappa_i$ and $n \geq 0$, there are $\binom{N-1-\kappa_i}{n} \binom{\kappa_i}{\omega}$ permutations σ such that $n_\sigma = n + \omega + 1$, $\sigma_i = 1$, and $\Delta_{\sigma,i} = \omega$. From this we get

$$\begin{aligned} \sum_{i \in \mathcal{V}} \sum_{n=0}^N (\tan \vartheta)^{2n} \sum_{\substack{\sigma | n_\sigma = n \\ \sigma_i = 1}} \cos(\Delta_{\sigma,i} t) &= \\ \tan^2 \vartheta \sum_{i \in \mathcal{V}} \Re \left\{ \sum_{\omega=0}^{\kappa_i} \binom{\kappa_i}{\omega} (e^{it} \tan^2 \vartheta)^\omega \right\} \times \\ \left[\sum_{n=0}^{N-1-\kappa_i} \binom{N-1-\kappa_i}{n} (\tan^2 \vartheta)^n \right], \end{aligned}$$

and

$$\sum_{i \in \mathcal{V}} \sum_{n=0}^N (\tan \vartheta)^{2n} \sum_{\substack{\sigma | n_\sigma = n \\ \sigma_i = 1}} \cos(\Delta_{\sigma, i} t) = \tan^2 \vartheta \sum_{i \in \mathcal{V}} \Re \left\{ (1 + e^{it} \tan^2 \vartheta)^{\kappa_i} \right\} \times (1 + \tan^2 \vartheta)^{N-1-\kappa_i},$$

The term in the sum over i only depends on κ_i so, if we note $m_{\mathcal{G}}(\kappa)$ the number of vertices of degree κ in \mathcal{G} , we obtain (20).

2. Extensions to quadratic observables

Using the same setup, but measuring the expectation value of the Ising Hamiltonian instead of the occupation, further insight on the graph can be obtained. In particular, correlation functions appear explicitly. The

expectation value of the observable is given by

$$\begin{aligned} \langle \hat{\mathcal{H}}_I(t) \rangle &= \sum_{(i,j) \in \mathcal{E}} \langle \hat{n}_i \hat{n}_j \rangle(t) \\ &= 4 \sin^2 \vartheta \cos^2 \vartheta |\mathcal{E}| + \\ &\quad 2 \sin^2 \vartheta (\cos \vartheta)^{2N+2} \sum_{\mathcal{V}' \subset \mathcal{V}} \sum_{(i,j) \in \mathcal{E}} \Re \left\{ f_{n'_i, n'_j}(t) \right\}, \end{aligned}$$

where the sum runs over all subgraphs $\mathcal{V}' \subset \mathcal{V}$, $n'_i = |\{k \in \mathcal{V}' | (i, k) \in \mathcal{E}\}|$ is the number of neighbors of i in \mathcal{V}' , and

$$\begin{aligned} f_{n,m}(t) &= e^{i(1+n+m)t} w(t)^2 + e^{i(n-m)t} |w(t)|^2 \\ &\quad - 2(e^{int} + e^{imt}) w(t), \end{aligned}$$

with $w(t) = (1 + \tan^2 \vartheta e^{it})^{-1}$.

3. Extension to a generic Ising model

We can extend the computation presented in III to the case of a graph with labeled vertices and/or weighted edges. For a given graph $\mathcal{G} = (\mathcal{V}, \mathcal{E})$, with vertex labels $\{h_i\}_{i \in \mathcal{V}}$ and edge labels $\{J_{ij}\}_{(i,j) \in \mathcal{E}}$ ⁹, let us consider a set of $N = |\mathcal{V}|$ qubits interacting with the Hamiltonian

$$\hat{\mathcal{H}}_{\mathcal{G}} = \sum_{(i,j) \in \mathcal{E}} J_{ij} \hat{\sigma}_i^z \hat{\sigma}_j^z + \sum_{i \in \mathcal{V}} h_i \hat{\sigma}_i^z. \quad (\text{A3})$$

In this case, the procedure described in III leads to a more generic version of (20) :

$$n(t) = 2 \sin^2 \vartheta \cos^2 \vartheta \sum_{i \in \mathcal{V}} \Re \left\{ 1 - e^{ih_i t} \prod_{j \in \mathcal{V}} (\cos^2 \vartheta + \sin^2 \vartheta e^{iJ_{ij} t}) \right\} \quad (\text{A4})$$

$$= 2N \sin^2 \vartheta \cos^2 \vartheta + 2 \sum_{\tilde{\mathcal{V}} \subset \mathcal{V}} (\cos \vartheta)^{2(N-|\tilde{\mathcal{V}}|+1)} (\sin \vartheta)^{2|\tilde{\mathcal{V}}|+2} \sum_{i \in \mathcal{V}} \cos \left[\left(h_i + \sum_{j \in \tilde{\mathcal{V}}} J_{ij} \right) t \right]. \quad (\text{A5})$$

For a given $i \in \mathcal{V}$, we note $\mathcal{V}_i^1 = \{j \in \mathcal{V} | (i, j) \in \mathcal{E}\}$ the set of neighbors of i , and $\mathcal{V}_i^0 = \{j \in \mathcal{V} | (i, j) \notin \mathcal{E}\} = \mathcal{V} \setminus \mathcal{V}_i^1$ its complement in \mathcal{V} , such that

$$n(t) = 2N \sin^2 \vartheta \cos^2 \vartheta + 2 \cos^2 \vartheta \sin^2 \vartheta \sum_{i \in \mathcal{V}} \cos^{2\kappa_i} \vartheta \sum_{\tilde{\mathcal{V}}^1 \subset \mathcal{V}_i^1} (\tan \vartheta)^{2|\tilde{\mathcal{V}}^1|} \cos \left[\left(h_i + \sum_{j \in \tilde{\mathcal{V}}^1} J_{ij} \right) t \right].$$

The Fourier transform would then have peaks at $k =$

$h_i + \sum_{j \in \tilde{\mathcal{V}}_i} J_{ij}$, where $\tilde{\mathcal{V}}_i \subset \mathcal{V}_i^1$ is any subset of the neighbourhood of i , with weight $\propto [(\sin \vartheta)^{|\tilde{\mathcal{V}}^1|} (\cos \vartheta)^{\kappa_i - |\tilde{\mathcal{V}}^1|}]^2$

⁹ For any $(i, j) \in \mathcal{V}^2$ such that $(i, j) \notin \mathcal{E}$, we set $J_{ij} = 0$.

4. Quadratic observables

Even with an Ising graph Hamiltonian, further information can be reached. We consider here the graph Hamiltonian to be the most generic Ising Hamiltonian

$$\hat{\mathcal{H}}_{\mathcal{G}} = \sum_{i < j} J_{ij} \hat{n}_i \hat{n}_j - \sum_i h_i \hat{n}_i \quad (\text{A6})$$

$$\langle n_{v_1} n_{v_2} \rangle(t) = 4 \sin^4 \vartheta \cos^4 \vartheta \Re \left\{ 1 - e^{ih_{v_1} t} w_{v_1 v_2}(t)^{-1} \prod_{v \in \mathcal{V}} w_{v_1 v}(t) - e^{ih_{v_2} t} w_{v_1 v_2}(t)^{-1} \prod_{v \in \mathcal{V}} w_{v_2 v}(t) + \frac{1}{2} e^{i(h_{v_1} + h_{v_2} + J_{v_1 v_2})t} w_{v_1 v_2}(t)^{-2} \prod_{v \in \mathcal{V}} w_v^+(t) + \frac{1}{2} e^{i(h_{v_1} - h_{v_2})t} |w_{v_1 v_2}(t)|^{-2} \prod_{v \in \mathcal{V}} w_v^-(t), \right\}$$

where

$$\begin{cases} w_{vv'}(t) &= \cos^2 \vartheta + \sin^2 \vartheta e^{iJ_{vv'} t} \\ w_v^\pm(t) &= \cos^2 \vartheta + \sin^2 \vartheta e^{i(J_{v_1 v} \pm J_{v_2 v})t} \end{cases} \quad (\text{A7})$$

Appendix B: Classical graph kernels

We briefly introduce here the classical kernels used for benchmark comparison, the Random Walk kernel [36] and the Graphlet Subsampling [34, 35] kernel.

1. Random Walk kernel

The random walk kernel aims at counting the number of random walks of different sizes between two graphs. Given $\mathcal{G} = (\mathcal{V}, \mathcal{E})$ and $\mathcal{G}' = (\mathcal{V}', \mathcal{E}')$ we define the product graph \mathcal{G}_\times as the graph with the set of vertices $\mathcal{V}_\times = \{(v, v') \in \mathcal{V} \times \mathcal{V}'\}$ and the set of edges $\mathcal{E}_\times = \{(e, e') \in \mathcal{E} \times \mathcal{E}'\}$. We denote then A_\times the adjacency matrix of the product graph. The geometric random walk kernel for a positive weight λ is defined as

$$k(\mathcal{G}, \mathcal{G}') = \sum_{p, q=1}^{|\mathcal{V}_\times|} \left[\sum_{l=0}^{\infty} \lambda^l A_\times^l \right]_{pq} = e^T (I - \lambda A_\times)^{-1} e, \quad (\text{B1})$$

where e is the vector full of 1s and I is the identity matrix. This kernel is only defined when λ is smaller than the inverse of the biggest eigenvalue of A_\times in order to allow convergence. This implies that small values of λ are tested in practice, which makes the contribution of long random walks vanish and limits the ability to capture complex features.

By measuring quadratic (and higher order) observables, one can extract information about the subgraphs of the system. For example, if one were to measure the *pure* Ising energy, (i.e. $\hat{\mathcal{O}} = \sum_{(i,j) \in \mathcal{E}} \hat{n}_i \hat{n}_j$)

2. Graphlet Subsampling kernel

Let G_k be the set of all possible graphlets of size k . For a given graph \mathcal{G} , we define $f_k(\mathcal{G})$ the vector such that the i -th component is the number of graphlets isomorphic to the i -th element of G_k normalized by the total number of graphlets of \mathcal{G} . The kernel is then defined by

$$k(\mathcal{G}, \mathcal{G}') = f_k(\mathcal{G})^T f_k(\mathcal{G}') \quad (\text{B2})$$

An exact evaluation of this kernel requires an exhaustive enumeration of the graphlets of each graph, which requires $\mathcal{O}(n^k)$ operations since there are $\binom{n}{k}$ graphlets in \mathcal{G} , n being the number of vertices. We resort then to randomly sampling a fixed number of graphlets in the graph, which leads to a good approximation (as described in [35]).

Appendix C: Bayesian Optimization

We are interested in the problem of finding the maximum of a function $f : \mathcal{X} \rightarrow \mathbb{R}$ where \mathcal{X} is a space of parameters, and f is a costly function to evaluate. In our case \mathcal{X} would be the space of parameters \mathbf{A} , and f would be the mean of the accuracy score in a cross-validation on a particular dataset. One way to do so is the bayesian optimization, which we will briefly summarize in this section [60].

Since the function f is very costly to evaluate, we build a model that approximates it. This model is called a surrogate function noted \tilde{f} , and is usually a gaussian process. A gaussian process \mathcal{GP} is completely defined by a mean function $\mu(x)$ and a covariance kernel $k(x, x')$ such that for any collection of points (x_1, \dots, x_n) , the vector $[\mathcal{GP}(x_1), \dots, \mathcal{GP}(x_n)]$ follows a multivariate normal of means $[\mu(x_1), \dots, \mu(x_n)]$ and covariance matrix given by the entries $k(x_i, x_j)$.

The kernel used is the Matérn kernel[61] given by

$$k(x, x') = \alpha_0 \frac{2^{1-\nu}}{\Gamma(\nu)} (\sqrt{2\nu} \|x - x'\|)^\nu K_\nu(\sqrt{2\nu} \|x - x'\|) \quad (\text{C1})$$

where Γ is the gamma function, K_ν is the modified Bessel function, and $\|x - x'\|^2 = \sum_i \alpha_i (x_i - x'_i)^2$ is a weighted norm.

For the multikernel learning, the kernel used is the Gaussian Radial Basis kernel:

$$k(x, x') = \alpha_0 \exp(\|x - x'\|^2) \quad (\text{C2})$$

where $\|x - x'\|^2 = \sum_i \alpha_i (x_i - x'_i)^2$ is a weighted norm.

Given some observations of f , the objective is to find the best surrogate function \tilde{f} . One then has to define an acquisition function $\alpha(x)$ that will give the information on where to perform the next evaluation of f . One commonly used acquisition function is the lower confidence bound defined by $\alpha(x) = \mu(x) + \kappa\sigma(x)$. κ is a positive parameters representing the trade-off between exploitation and exploration.

Instead of sequentially evaluating the function and updating the gaussian process, one can use a parallelised version of the algorithm [62]. Instead of minimizing an acquisition function, the next point to evaluate is determined by the minimum of a sample of the gaussian process. The surrogate function is then updated by batches.

Algorithm 1: Bayesian optimization with gaussian surrogate

```

Observe  $f$  at  $n_0$  points;
Fit the gaussian process  $\tilde{f}$ ;
for  $n_0 \leq i \leq N$  do
    Find  $x_i^* = \text{argmin}_x \alpha(x)$ 
    Evaluate  $f$  at  $x_i^*$ ;
    Update  $\tilde{f}$  with the new couple  $x_i^*, f(x_i^*)$ 
end
Result:  $\text{argmin}(f(x_1^*), \dots, f(x_N^*))$ 

```

Appendix D: Multiple kernel learning

We explore here a postprocessing strategy to improve the score. Multikernel learning is the idea of combining several kernels to construct a better one [38]. Such a combination can be made in several way, the most common ones being by linear combination or product. Given a family of kernels (K_1, \dots, K_R) , we are interested in building the new kernel

$$K_{\mathbf{p}} = \sum_{i=1}^R p_i K_i, \quad (\text{D1})$$

Algorithm 2: Parallel bayesian optimization with gaussian surrogate and k workers

```

Observe  $f$  at  $n_0$  points;
Fit the gaussian process  $\tilde{f}$ ;
for  $n_0 \leq i \leq N$  do
    for each worker  $j$  do
        Sample  $\hat{f}$  from  $\tilde{f}$ 
        Find  $x_j^* = \text{argmin}_x \hat{f}(x)$ 
        Evaluate  $f$  at  $x_j^*$ ;
    end
    Aggregate the values  $x_j^*, f(x_j^*)$  for each worker;
    Update  $\tilde{f}$ ;
end
Result:  $\text{argmin}(f(x_1^*), \dots, f(x_{kN}^*))$ 

```

where $\mathbf{p} = (p_1, \dots, p_R)$ is a R -uplet of non-negative numbers. For a fixed \mathbf{p} a new kernel is created, and a model can be trained on it. The question is whether there exists a \mathbf{p} such that the model given by $K_{\mathbf{p}}$ is better than any model given by the individuals kernels.

In our case, a kernel defined for each parameter Λ . R values of the parameters are chosen and an optimal combination of their corresponding kernels is determined. The entries of \mathbf{p} are bounded between 0 and 1, and the best value is found again by bayesian optimization. This method uses the results obtained previously by the quantum evolution, and can be done classically without any further consumption of quantum resources.

The procedure is tested in different settings. For each Hamiltonian type Ising or XY, up to $R = 10$ different kernels are used, as described in V, Two ways of selecting these kernels are tested. In the first one, R kernels are chosen randomly while in the second approach, only the R best performing kernels are considered. The optimization is performed by making $50 \times n_{kernel}$ calls and $20 \times n_{kernel}$ initial evaluations where n_{kernel} is the number of individual kernels to consider. The results are shown in figure 7. The procedure is most of the time successful — *i.e* a combination of individual kernels manages to get a better score than the best of single kernels —, and the score improves with the number of kernels combined, as one would expect theoretically. However, because of the limitations of the optimization procedures, it is not always the case here. For IMDB-BINARY, PROTEINS, Fingerprints a better score is consistently reached for almost every configuration. For NCI1, only the 2 best XY kernels and the best Ising kernels can be combined to produce a better score. Random Ising kernels for IMDB-MULTI and random kernels for PTC_FM also fail. It is interesting to note that the best combination of random kernels never beats the best individual kernel with optimized parameters, except in the case of IMDB-BINARY where the best combination of 4 and 6 random Ising kernels beats the best XY kernel.

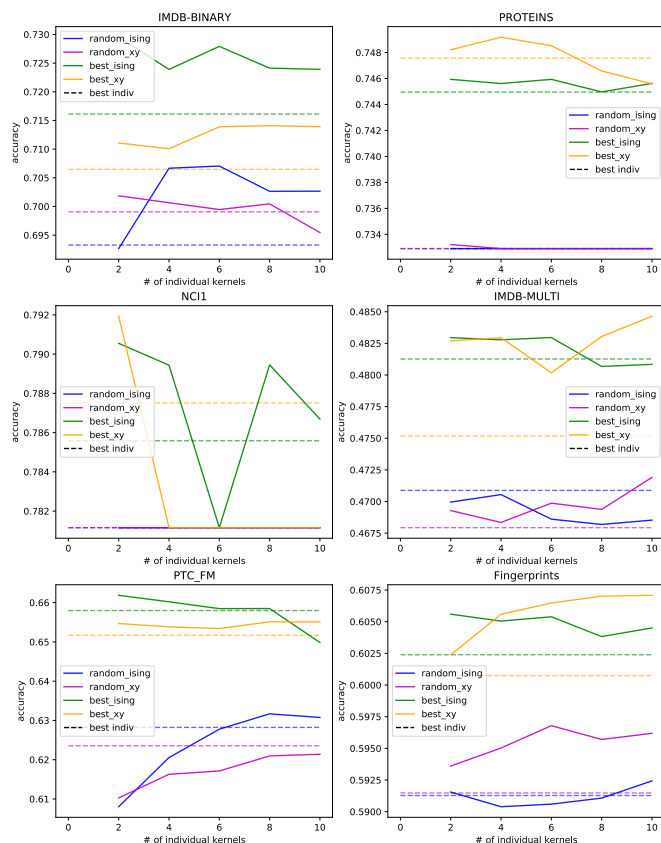


FIG. 7. Accuracy obtained after multiple kernel learning as a function of the number of individual kernels. Each panel corresponds to a different dataset. In each one, the solid green (yellow) curve is obtained by combining the R best performing kernels in the Ising (XY) scheme, and the solid blue (purple) is obtained by combining R random kernels in the Ising (XY) scheme. For each of these curves, a dotted line of the same color represents the accuracy of the best performing kernel among the ones that are combined.

-
- [1] Alexandre Varnek and Igor Baskin. Machine learning methods for property prediction in chemoinformatics: Quo vadis? *Journal of Chemical Information and Modeling*, 52(6):1413–1437, 2012. doi:10.1021/ci200409x. URL <https://doi.org/10.1021/ci200409x>. PMID: 22582859.
 - [2] Justin Gilmer, Samuel S. Schoenholz, Patrick F. Riley, Oriol Vinyals, and George E. Dahl. Neural message passing for quantum chemistry. In Doina Precup and Yee Whye Teh, editors, *Proceedings of the 34th International Conference on Machine Learning*, volume 70 of *Proceedings of Machine Learning Research*, pages 1263–1272. PMLR, 06–11 Aug 2017. URL <http://proceedings.mlr.press/v70/gilmer17a.html>.
 - [3] Giulia Muzio, Leslie O’Bray, and Karsten Borgwardt. Biological network analysis with deep learning. *Briefings in Bioinformatics*, 22(2):1515–1530, 11 2020. ISSN 1477-4054. doi:10.1093/bib/bbaa257. URL <https://doi.org/10.1093/bib/bbaa257>.
 - [4] K. M. Borgwardt, C. S. Ong, S. Schönauer, S. V. Vishwanathan, A. J. Smola, and H. P. Kriegel. Protein function prediction via graph kernels. *Bioinformatics*, 21, 2005. doi:10.1093/bioinformatics/bti1007.
 - [5] John Scott. Social network analysis: developments, advances, and prospects. *Social Network Analysis and Mining*, 1(1), 01 2011. doi:10.1007/s13278-010-0012-6. URL <https://doi.org/10.1007/s13278-010-0012-6>.
 - [6] Zaïd Harchaoui and Francis Bach. Image classification with segmentation graph kernels. In *2007 IEEE Conference on Computer Vision and Pattern Recognition*, pages 1–8. IEEE, 2007.
 - [7] Giannis Nikolentzos, Polykarpos Meladianos, François Rousseau, Yannis Stavrakas, and Michalis Vazirgiannis. Shortest-path graph kernels for document similarity. In *Proceedings of the 2017 Conference on Empirical Methods in Natural Language Processing*, pages 1890–1900, 2017.
 - [8] Goran Glavaš and Jan Šnajder. Recognizing identical events with graph kernels. In *Proceedings of the 51st An-*

- nual Meeting of the Association for Computational Linguistics (Volume 2: Short Papers)*, pages 797–803, 2013.
- [9] Pierre Latouche and Fabrice Rossi. Graphs in machine learning: an introduction. *European Symposium on Artificial Neural Networks, Computational Intelligence and Machine Learning (ESANN)*, pages 207–218, April 2015.
- [10] Niels M. Kriege, Fredrik D. Johansson, and Christopher Morris. A survey on graph kernels. *Applied Network Science*, 5(6), 2020. doi:10.1007/s41109-019-0195-3. URL <https://doi.org/10.1007/s41109-019-0195-3>.
- [11] Karsten M. Borgwardt, M. Elisabetta Ghisu, Felipe Llinares-López, Leslie O’Bray, and Bastian Rieck. Graph kernels: State-of-the-art and future challenges. *Foundations and Trends in Machine Learning*, 13(5-6), 2020. doi:10.1561/22000000076. URL <https://doi.org/10.1561/22000000076>.
- [12] B. Schölkopf and A. J. Smola. *Learning with Kernels: Support Vector Machines, Regularization, Optimization, and Beyond*. The MIT Press, 2001.
- [13] Maria Schuld and Nathan Killoran. Quantum machine learning in feature hilbert spaces. *Phys. Rev. Lett.*, 122:040504, Feb 2019. doi:10.1103/PhysRevLett.122.040504. URL <https://link.aps.org/doi/10.1103/PhysRevLett.122.040504>.
- [14] Vojtěch Havlíček, Antonio D. Córcoles, Kristan Temme, Aram W. Harrow, Abhinav Kandala, Jerry M. Chow, and Jay M. Gambetta. Supervised learning with quantum-enhanced feature spaces. *Nature*, 567(7747):209–212, 2019. doi:10.1038/s41586-019-0980-2. URL <https://doi.org/10.1038/s41586-019-0980-2>.
- [15] Kaito Kishi, Takahiko Satoh, Rudy Raymond, Naoki Yamamoto, and Yasubumi Sakakibara. Graph kernels encoding features of all subgraphs by quantum superposition, 2021.
- [16] Guillaume Verdon, Trevor McCourt, Enxhell Luzhnic, Vikash Singh, Stefan Leichenauer, and Jack Hidary. Quantum Graph Neural Networks. *arXiv e-prints*, art. arXiv:1909.12264, September 2019.
- [17] Luca Rossi, Andrea Torsello, and Edwin Hancock. Measuring graph similarity through continuous-time quantum walks and the quantum jensen-shannon divergence. *Physical Review E*, 91:022815, 02 2015. doi:10.1103/PhysRevE.91.022815.
- [18] Lu Bai, Luca Rossi, Peng Ren, Zhihong Zhang, and Edwin R. Hancock. A Quantum Jensen-Shannon Graph Kernel Using Discrete-Time Quantum Walks. In Cheng-Lin Liu, Bin Luo, Walter G. Kropatsch, and Jian Cheng, editors, *Graph-Based Representations in Pattern Recognition*, pages 252–261, Cham, 2015. Springer International Publishing. ISBN 978-3-319-18224-7. URL https://doi.org/10.1007/978-3-319-18224-7_25.
- [19] Maria Schuld, Kamil Brádler, Robert Israel, Daiqin Su, and Brajesh Gupta. Measuring the similarity of graphs with a gaussian boson sampler. *Phys. Rev. A*, 101:032314, Mar 2020. doi:10.1103/PhysRevA.101.032314. URL <https://link.aps.org/doi/10.1103/PhysRevA.101.032314>.
- [20] Edward Farhi, Jeffrey Goldstone, and Sam Gutmann. A Quantum Approximate Optimization Algorithm. *arXiv e-prints*, art. arXiv:1411.4028, Nov 2014.
- [21] J Werschnik and E K U Gross. Quantum optimal control theory. *Journal of Physics B: Atomic, Molecular and Optical Physics*, 40(18):R175–R211, sep 2007. doi:10.1088/0953-4075/40/18/r01. URL <https://doi.org/10.1088/0953-4075/40/18/r01>.
- [22] Hendrik Weimer, Igor Müller, Markus Lesanovsky, Peter Zoller, and Hans Peter Büchler. A rydberg quantum simulator. *Nature Physics*, 6:382–388, Mar 2010. doi:10.1038/nphys1614. URL <https://doi.org/10.1038/nphys1614>.
- [23] Hannes Bernien, Sylvain Schwartz, Alexander Keesling, Harry Levine, Ahmed Omran, Hannes Pichler, Soonwon Choi, Alexander S. Zibrov, Manuel Endres, Markus Greiner, Vladan Vuletić, and Mikhail D. Lukin. Probing many-body dynamics on a 51-atom quantum simulator. *Nature*, 551(7682):579–584, November 2017. doi:10.1038/nature24622.
- [24] Henning Labuhn, Daniel Barredo, Sylvain Ravets, Sylvain de Léséleuc, Tommaso Macrì, Thierry Lahaye, and Antoine Browaeys. Tunable two-dimensional arrays of single Rydberg atoms for realizing quantum Ising models. *Nature*, 534(7609):667–670, Jun 2016. doi:10.1038/nature18274.
- [25] Giannis Nikolentzos, Giannis Sigidis, and Michalis Vazirgiannis. Graph kernels: A survey, 2019.
- [26] C. Bishop. *Pattern Recognition and Machine Learning*. Springer-Verlag New York, Cambridge, 2006.
- [27] Christopher Morris, Nils M. Kriege, Franka Bause, Kristian Kersting, Petra Mutzel, and Marion Neumann. TUDataset: A collection of benchmark datasets for learning with graphs. In *ICML 2020 Workshop on Graph Representation Learning and Beyond (GRL+ 2020)*, 2020. URL www.graphlearning.io.
- [28] Pornntiwa Pawara, Emmanuel Okafor, Marc Groefsema, Sheng He, Lambert R.B. Schomaker, and Marco A. Wiering. One-vs-one classification for deep neural networks. *Pattern Recognition*, 108:107528, 2020. ISSN 0031-3203. doi:https://doi.org/10.1016/j.patcog.2020.107528. URL <https://www.sciencedirect.com/science/article/pii/S0031320320303319>.
- [29] J. Lin. Divergence measures based on the shannon entropy. *IEEE Transactions on Information Theory*, 37(1):145–151, 1991. doi:10.1109/18.61115.
- [30] P. Erdős and A. Rényi. On random graphs. i. *Publications Mathematicae*, 6, 1959.
- [31] Nino Shervashidze, Pascal Schweitzer, Erik Jan van Leeuwen, Kurt Mehlhorn, and Karsten M. Borgwardt. Weisfeiler-lehman graph kernels. *Journal of Machine Learning Research*, 12(77):2539–2561, 2011. URL <http://jmlr.org/papers/v12/shervashidze11a.html>.
- [32] Lu Bai. *Information Theoretic Graph Kernels*. Theses, Department of Computer Science, University of York, May 2014.
- [33] Andrew M. Childs, Richard Cleve, Enrico Deotto, Edward Farhi, Sam Gutmann, and Daniel A. Spielman. Exponential algorithmic speedup by a quantum walk. In *Proceedings of the Thirty-Fifth Annual ACM Symposium on Theory of Computing*, STOC ’03, page 59–68, New York, NY, USA, 2003. Association for Computing Machinery. ISBN 1581136749. doi:10.1145/780542.780552. URL <https://doi.org/10.1145/780542.780552>.
- [34] Nataša Pržulj. Biological network comparison using graphlet degree distribution. *Bioinformatics*, 23(2):e177–e183, 01 2007. ISSN 1367-4803. doi:10.1093/bioinformatics/btl301. URL <https://doi.org/10.1093/bioinformatics/btl301>.
- [35] Nino Shervashidze, SVN Vishwanathan, Tobias Petri, Kurt Mehlhorn, and Karsten Borgwardt. Efficient

- graphlet kernels for large graph comparison. In David van Dyk and Max Welling, editors, *Proceedings of the Twelfth International Conference on Artificial Intelligence and Statistics*, volume 5 of *Proceedings of Machine Learning Research*, pages 488–495, Hilton Clearwater Beach Resort, Clearwater Beach, Florida USA, 16–18 Apr 2009. PMLR. URL <http://proceedings.mlr.press/v5/shervashidze09a.html>.
- [36] S.V.N. Vishwanathan, Nicol N. Schraudolph, Risi Kondor, and Karsten M. Borgwardt. Graph kernels. *Journal of Machine Learning Research*, 11(40):1201–1242, 2010. URL <http://jmlr.org/papers/v11/vishwanathan10a.html>.
- [37] Giannis Siglidis, Giannis Nikolentzos, Stratis Limnios, Christos Giatsidis, Konstantinos Skianis, and Michalis Vazirgiannis. Grakel: A graph kernel library in python. *Journal of Machine Learning Research*, 21(54):1–5, 2020.
- [38] Mehmet Gönen and Ethem Alpaydm. Multiple kernel learning algorithms. *The Journal of Machine Learning Research*, 12:2211–2268, 2011.
- [39] C. Monroe, W. C. Campbell, L. M. Duan, Z. X. Gong, A. V. Gorshkov, P. W. Hess, R. Islam, K. Kim, N. M. Linke, G. Pagano, P. Richerme, C. Senko, and N. Y. Yao. Programmable quantum simulations of spin systems with trapped ions. *Reviews of Modern Physics*, 93(2):025001, April 2021. doi:10.1103/RevModPhys.93.025001.
- [40] Natalia G Berloff, Kirill Kalinin, Matteo Silva, Wolfgang Langbein, and Pavlos G Lagoudakis. Realizing the xy hamiltonian in polariton simulators. *Nature Materials*, 16:1120–1126, 2017. URL <https://doi.org/10.1038/nmat4971>.
- [41] Antoine Browaeys and Thierry Lahaye. Many-body physics with individually controlled rydberg atoms. *Nature Physics*, 16(2):132–142, Feb 2020. ISSN 1745-2481. doi:10.1038/s41567-019-0733-z. URL <https://doi.org/10.1038/s41567-019-0733-z>.
- [42] M. Saffman, T. G. Walker, and K. Mølmer. Quantum information with Rydberg atoms. *Reviews of Modern Physics*, 82(3):2313–2363, Jul 2010. doi:10.1103/RevModPhys.82.2313.
- [43] M. Saffman. Quantum computing with atomic qubits and Rydberg interactions: progress and challenges. *Journal of Physics B Atomic Molecular Physics*, 49(20):202001, October 2016. doi:10.1088/0953-4075/49/20/202001.
- [44] Daniel Barredo, Sylvain de Léséleuc, Vincent Lienhard, Thierry Lahaye, and Antoine Browaeys. An atom-by-atom assembler of defect-free arbitrary two-dimensional atomic arrays. *Science*, 354(6315):1021–1023, November 2016. ISSN 0036-8075, 1095-9203. doi:10.1126/science.aah3778. URL <https://science.sciencemag.org/content/354/6315/1021>.
- [45] Manuel Endres, Hannes Bernien, Alexander Keesling, Harry Levine, Eric R. Anschuetz, Alexandre Krajenbrink, Crystal Senko, Vladan Vuletic, Markus Greiner, and Mikhail D. Lukin. Atom-by-atom assembly of defect-free one-dimensional cold atom arrays. *Science*, 354(6315):1024–1027, November 2016. ISSN 0036-8075, 1095-9203. doi:10.1126/science.aah3752. URL <https://science.sciencemag.org/content/354/6315/1024>.
- [46] Daniel Barredo, Vincent Lienhard, Sylvain de Léséleuc, Thierry Lahaye, and Antoine Browaeys. Synthetic three-dimensional atomic structures assembled atom by atom. *Nature*, 561(7721):79–82, September 2018. ISSN 1476-4687. doi:10.1038/s41586-018-0450-2. URL <https://www.nature.com/articles/s41586-018-0450-2>.
- [47] Loïc Henriët, Lucas Beguin, Adrien Signoles, Thierry Lahaye, Antoine Browaeys, Georges-Olivier Raymond, and Christophe Jurczak. Quantum computing with neutral atoms. *Quantum*, 4:327, September 2020. ISSN 2521-327X. doi:10.22331/q-2020-09-21-327. URL <https://doi.org/10.22331/q-2020-09-21-327>.
- [48] M. Morgado and S. Whitlock. Quantum simulation and computing with Rydberg-interacting qubits. *arXiv e-prints*, art. arXiv:2011.03031, November 2020.
- [49] I. I. Beterov. Quantum Computers Based on Cold Atoms. *Optoelectronics, Instrumentation and Data Processing*, 56(4):317–324, July 2020. doi:10.3103/S8756699020040020.
- [50] Xiaoling Wu, Xinhui Liang, Yaoqi Tian, Fan Yang, Cheng Chen, Yong-Chun Liu, Meng Khooon Tey, and Li You. A concise review of Rydberg atom based quantum computation and quantum simulation. *arXiv e-prints*, art. arXiv:2012.10614, December 2020.
- [51] Peter Schauß, Johannes Zeiher, Takeshi Fukuhara, Sebastian Hild, Marc Cheneau, Tommaso Macrì, Thomas Pohl, Immanuel Bloch, and Christian Groß. Crystallization in ising quantum magnets. *Science*, 347(6229):1455–1458, 2015.
- [52] Henning Labuhn, Daniel Barredo, Sylvain Ravets, Sylvain De Léséleuc, Tommaso Macrì, Thierry Lahaye, and Antoine Browaeys. Tunable two-dimensional arrays of single rydberg atoms for realizing quantum ising models. *Nature*, 534(7609):667–670, 2016.
- [53] Sylvain de Léséleuc, Sebastian Weber, Vincent Lienhard, Daniel Barredo, Hans Peter Büchler, Thierry Lahaye, and Antoine Browaeys. Accurate mapping of multilevel rydberg atoms on interacting spin-1/2 particles for the quantum simulation of ising models. *Phys. Rev. Lett.*, 120:113602, Mar 2018. doi:10.1103/PhysRevLett.120.113602. URL <https://link.aps.org/doi/10.1103/PhysRevLett.120.113602>.
- [54] Daniel Barredo, Henning Labuhn, Sylvain Ravets, Thierry Lahaye, Antoine Browaeys, and Charles S. Adams. Coherent excitation transfer in a spin chain of three rydberg atoms. *Phys. Rev. Lett.*, 114:113002, Mar 2015. doi:10.1103/PhysRevLett.114.113002. URL <https://link.aps.org/doi/10.1103/PhysRevLett.114.113002>.
- [55] A. Piñeiro Orioli, A. Signoles, H. Wildhagen, G. Günter, J. Berges, S. Whitlock, and M. Weidemüller. Relaxation of an isolated dipolar-interacting rydberg quantum spin system. *Phys. Rev. Lett.*, 120:063601, Feb 2018. doi:10.1103/PhysRevLett.120.063601. URL <https://link.aps.org/doi/10.1103/PhysRevLett.120.063601>.
- [56] Sylvain de Léséleuc, Vincent Lienhard, Pascal Scholl, Daniel Barredo, Sebastian Weber, Nicolai Lang, Hans Peter Büchler, Thierry Lahaye, and Antoine Browaeys. Observation of a symmetry-protected topological phase of interacting bosons with rydberg atoms. *Science*, 365(6455):775–780, 2019. ISSN 0036-8075. doi:10.1126/science.aav9105. URL <https://science.sciencemag.org/content/365/6455/775>.
- [57] Henrique Silvério, Sebastián Grijalva, Constantin Dalyac, Lucas Leclerc, Peter J. Karalekas, Nathan Shammah, Mourad Beji, Louis-Paul Henry, and Loïc Henriët. Pulser: An open-source package for the design of pulse sequences in programmable neutral-atom arrays, 2021.

- [58] Ewin Tang. Quantum-inspired classical algorithms for principal component analysis and supervised clustering. *arXiv e-prints*, art. arXiv:1811.00414, October 2018.
- [59] Juan Miguel Arrazola, Alain Delgado, Bhaskar Roy Bardhan, and Seth Lloyd. Quantum-inspired algorithms in practice. *Quantum*, 4:307, August 2020. ISSN 2521-327X. doi:10.22331/q-2020-08-13-307. URL <https://doi.org/10.22331/q-2020-08-13-307>.
- [60] Peter I. Frazier. A tutorial on bayesian optimization, 2018.
- [61] Bertil Matérn. *Spatial Variation*. Springer-Verlag, 1986.
- [62] Kirthevasan Kandasamy, Akshay Krishnamurthy, Jeff Schneider, and Barnabás Póczos. Parallelised bayesian optimisation via thompson sampling. In *International Conference on Artificial Intelligence and Statistics*, pages 133–142. PMLR, 2018.